JGR Atmospheres

RESEARCH ARTICLE
10.1029/2018JD029884

Distinct Propagation Characteristics of Intraseasonal Variability Over the Tropical West Pacific

Alex O. Gonzalez[1,2,3] **and Xianan Jiang**[1,2]

[1]Joint Institute for Regional Earth System Science and Engineering, University of California, Los Angeles, CA, USA, [2]Jet Propulsion Laboratory, California Institute of Technology, Pasadena, CA, USA, [3]Now at Department of Geological and Atmospheric Sciences, Iowa State University, Ames, IA, USA

Key Points:
- Strong interannual variability of intraseasonal OLR exists in the tropical WP, dominated by the MJO and a westward propagating mode (WPIM)
- MSE budgets show that the MJO and WPIM are driven by horizontal MSE advection and the seasonal distribution of low-level moisture and zonal wind

Correspondence to:
A. O. Gonzalez,
agon@iastate.edu

Citation:
Gonzalez, A. O., & Jiang, X. (2019). Distinct propagation characteristics of intraseasonal variability over the tropical west Pacific. *Journal of Geophysical Research: Atmospheres*, *124*, 5332–5351. https://doi.org/10.1029/2018JD029884

Received 23 OCT 2018
Accepted 4 APR 2019
Accepted article online 25 APR 2019
Published online 29 MAY 2019
Corrected 2 SEP 2019

This article was corrected on 2 SEP 2019. See the end of the full text for details.

Abstract Tropical intraseasonal variability, with the Madden-Julian oscillation (MJO) as its most prominent mode, exerts extensive influences on global weather extremes. It is found that strong interannual variability of intraseasonal convection exists in the west Pacific (WP), in the form of years with strong eastward propagation (i.e., associated with the MJO) and years with strong westward propagation. Years with strong westward propagation on intraseasonal timescales are dominated by a westward propagating intraseasonal mode (WPIM), which is the second leading intraseasonal mode after the MJO over the tropical WP. Initiated over the central Pacific, the WPIM exhibits slow equatorial westward propagation (5 m/s) with a period of 25 days and a spatial scale of zonal wave number 3–4. Unlike the MJO, the WPIM lacks a significant tilt with height in specific humidity and vertical velocity. A strong anticorrelation is found between MJO and WPIM activity on interannual timescales over the WP. Budget analyses of the moist static energy suggest that both modes are driven by horizontal moist static energy advection and that substantial differences in winter mean large-scale moisture and zonal winds largely define their distinct propagation behaviors. The WPIM is favored, while the MJO is suppressed when mean equatorial low-level easterlies between 150°E and 160°W are enhanced and equatorial mean low-level moisture is reduced near the Dateline and enhanced in the off-equatorial WP (110°–150°E). While the WPIM bears resemblance to low-frequency equatorial Rossby waves, a more detailed analysis must be conducted to affirm if they are the same phenomenon.

1. Introduction

Intraseasonal oscillations deserve special consideration in atmospheric and oceanic sciences because of their critical role as a *bridge* between weather and climate (Waliser et al., 2006; Zhang, 2013). The leading mode of tropical intraseasonal variability is the Madden-Julian oscillation (MJO; Madden & Julian, 1971, 1972). The MJO is characterized by oscillations in winds, pressure, and convection that typically initiate in the equatorial Indian Ocean and propagate slowly eastward at 5 m/s through the tropical Indian Ocean and west Pacific (Indo-Pacific) warm pool region. The circulation of the MJO is planetary in spatial scale but often has smaller-scale convective disturbances embedded within it (Dias et al., 2017; Hendon & Liebmann, 1994; Kikuchi & Takayabu, 2004; Kikuchi & Wang, 2010; Kiladis et al., 2009; Nakazawa, 1988). Through modulations in local atmospheric conditions and global teleconnections, the MJO can have wide-ranging impacts on extreme climate and weather events across the globe (e.g., Serra et al., 2014; Zhang, 2013). Even though it is well known that accurate MJO simulations are vital to improving extended-range weather prediction (e.g., Hurrell et al., 2009; Neena et al., 2014; Vitart et al., 2017; Vitart & Molteni, 2010), general circulation models have a notoriously difficult time modeling the MJO accurately (e.g., Ahn et al., 2017; Hung et al., 2013; Jiang, 2017; Jiang et al., 2015). The main reason that the MJO is so difficult to model has to do with a dearth of understanding many fundamental aspects of MJO physics. In fact, it has been said that the MJO is a *holy grail* of tropical atmospheric dynamics (Raymond, 2001).

Despite the shortcomings in our knowledge of the MJO's underlying physics, there has been considerable progress within the last decade or so. One core idea that has made significant headway in the community is that MJO precipitation is regulated primarily by atmospheric moisture, often referred to as moisture mode theory (Adames & Kim, 2016; Raymond & Fuchs, 2009; Sobel & Maloney, 2012, 2013; Yu & Neelin, 1994). Adopting this framework, many studies have found that anomalous column-integrated horizontal moist static energy (MSE) or moisture advection is crucial to the systematic eastward propagation

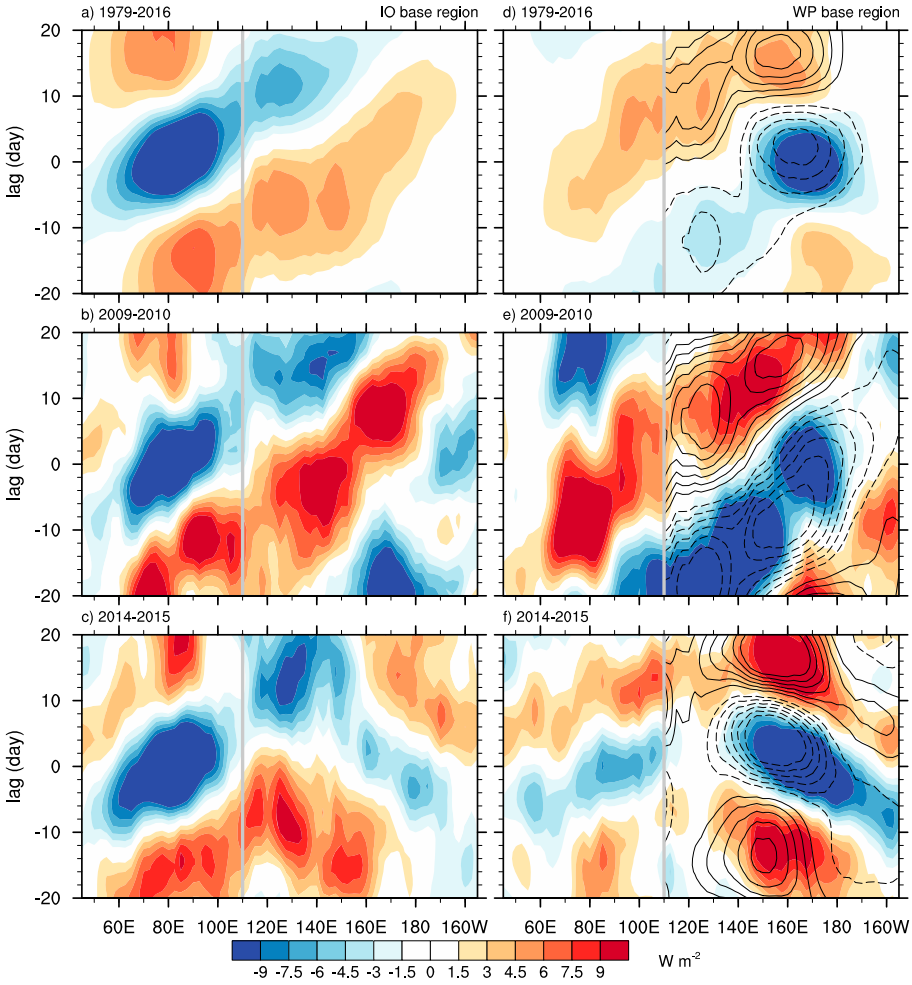

Figure 1. Longitude-lag diagrams of 10°S–10°N averaged unfiltered OLR anomalies lag regressed onto a 15–100-day band-pass-filtered OLR time series averaged over an Indian Ocean box (5°S–5°N, 75°–85°E, left panels) and a WP box (5°S–5°N, 165°–175°E, right panels) for November through April of (a, d) 1979–2016, (b, e) 2009–2010, and (c, f) 2014–2015. Overlaid in contour lines are 10°S–10°N averaged OLR anomalies reconstructed using the first two propagating modes of an EOF analysis over the WP (110°E–140°W) lag regressed onto the IO and WP time series in OLR (contour interval of 1 W/m^2), negative values dashed (zero line omitted). The gray vertical lines approximately denote the longitude where westward propagation ceases. All diagrams are multiplied by −1 standard deviation of the respective IO or WP OLR time series.

of the MJO (e.g., Adames & Wallace, 2015; Andersen & Kuang, 2012; Benedict et al., 2015; Cai et al., 2013; Chikira, 2014; Hsu & Li, 2012; Jiang, 2017; Kim et al., 2014; Kim et al., 2017; Maloney, 2009; Pritchard & Bretherton, 2014), although vertical advection has also been noted for playing a role (Hsu & Li, 2012; Sobel et al., 2014; Wang et al., 2017; Yokoi & Sobel, 2015). In particular, it is the horizontal advection of the seasonal mean moisture by the MJO winds in the lower troposphere that appears to be the most important contributor to total horizontal moisture advection (Adames & Wallace, 2015; Cai et al., 2013; Chikira, 2014; Gonzalez & Jiang, 2017; Hsu & Li, 2012; Jiang, 2017; Kim, 2017; Kim et al., 2017; Nasuno et al., 2015; Wolding et al., 2016).

While the eastward propagating MJO has received extensive attention in regard to intraseasonal variability, in this study we observe that convection on intraseasonal timescales exhibits strong interannual variations in propagation over the equatorial west Pacific (WP). In addition to years with strong MJO activity and eastward propagation, there are years when westward propagating intraseasonal features are more apparent than the MJO over the WP. For example, Figures 1a and 1d display anomalies of 10°S–10°N averaged unfiltered outgoing longwave radiation (OLR) lag regressed onto a 15–100-day band-pass-filtered Indian Ocean

(75°–85°E, 5°S–5°N) and WP (165°–175°E, 5°S–5°N) OLR time series during November through April of 1979–2016. Note that all signals in Figure 1 are multiplied by −1 standard deviation of the respective OLR time series. While systematic eastward OLR propagation of the MJO from the Indian Ocean to the WP is clearly evident based on the 1979–2016 long-term data, even more coherent eastward propagation of MJO convection over the WP is observed during particular winters, for example, 2009–2010 (Figures 1b and 1e). In contrast, distinct westward propagation of intraseasonal convection over the WP occurs during other winters, such as the 2014–2015 winter as shown in Figures 1c and 1f. An empirical orthogonal function (EOF) analysis is performed later that effectively identifies these eastward and westward propagation extremes, as illustrated in the black contour lines overlaid in Figures 1d–1f. Note that westward propagation mainly occurs over the WP but not so much over the Indian Ocean, where eastward propagation is still evident during winter 2014–2015. This behavior is possibly related to the *barrier* effects on the MJO propagation by the Maritime Continent (e.g., Kim et al., 2014; Salby & Hendon, 1994; Zhang & Ling, 2017). Westward propagating disturbances whose convection initiates just east of the Dateline and weakens over the Maritime Continent, similar to Figures 1d and 1f, exist during many other years in the 37 winter season (1979–2016) record of lag-regressed OLR anomalies (not shown). Overall, it is apparent that there is strong interannual variability of tropical intraseasonal convective propagation primarily over the WP. One might speculate that the westward propagating disturbances in Figure 1 are related to convectively coupled $n = 1$ equatorial Rossby (ER) waves since convectively coupled $n = 1$ ER waves tend to be most active over the central and WP and their variance peaks near periods of 25–30 days (e.g., Kiladis et al., 2009). As we discuss in more detail later, these westward propagating intraseasonal events do bear resemblance to convectively coupled low-frequency ER waves but a more exhaustive study of this comparison has to be conducted, which is beyond the immediate focus of this paper.

Even though the propagation mechanisms for ER waves are inherently described by the beta effect (i.e., dry dynamics; Matsuno, 1966), we still do not have a firm theoretical understanding of how coupling with moisture affects characteristics of westward propagating intraseasonal disturbances. Recent work by Fuchs and Raymond (2017) and Fuchs-Stone et al. (2019) has provided an idealized theory for how moisture affects both eastward and westward propagating intraseasonal oscillations for the MJO and convectively coupled ER waves, respectively. To this end, there has been a wealth of research on observations of convectively coupled ER waves (e.g., Keen, 1982; Kiladis et al., 1994; Kiladis & Wheeler, 1995; Kiladis et al., 2009; Roundy & Frank, 2004a; Wheeler & Kiladis, 1999); difficulties often arise, however, when trying to isolate ER waves because they have slow propagation speeds and may represent a standing component of the MJO (Roundy & Frank, 2004b). Westward propagating intraseasonal disturbances in OLR were also noted by the complementary studies of Roundy and Frank (2004a, 2004b). They emphasized that there often are cooperative nonlinear interactions between westward and eastward propagating intraseasonal oscillations due to wave reflection at preferred longitudinal locations, some of which are near coastlines or topography such as the Maritime Continent. Feng et al. (2015) illustrated that damped eastward propagation near the Maritime Continent region of many MJO events is often associated with arrival of 10–30-day westward propagating dry Rossby wave disturbances over the WP. These westward propagating ER waves tend to initiate over the eastern Pacific with two off-equatorial anticyclonic gyres near 20–25° latitude on both sides of the equator. DeMott et al. (2018) found similar dry westward propagating signals (10–30-day timescales) that cause many MJO events to dissipate near the Maritime Continent, and they discuss how the activity of these dry signals is highly modulated by interannual (La Niña versus El Niño) variations in background moisture gradients over the WP. The results in DeMott et al. (2018) could be relevant to the interannual variability seen in Figure 1 for years with strong eastward propagation and years with strong westward propagation.

In this study, we acquire a more holistic understanding of moisture mode theory that incorporates both eastward and westward intraseasonal propagating modes. We are motivated by the strong interannual variations in intraseasonal disturbances over the WP as shown in Figure 1. While many aspects of $n = 1$ ER waves have been studied in the literature, low-frequency westward propagating intraseasonal oscillations have not been fully exploited within the context of moisture mode theory and interannual variability of intraseasonal oscillations to the best of our knowledge. In addition to the characterization of detailed structures of the westward propagating events, we explore the physical processes responsible for them and their relationship to the eastward propagating MJO. In particular, important implications regarding the fundamental physics in regulating propagation of the intraseasonal variability are discussed based on these results. The outline

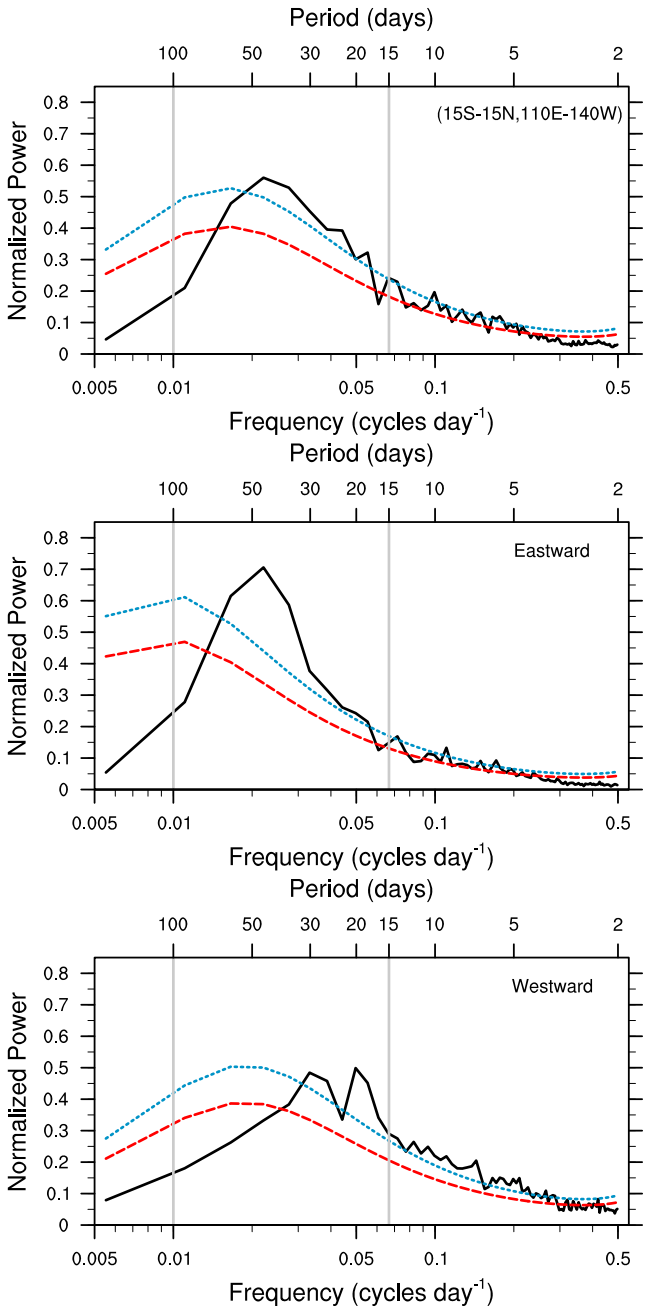

Figure 2. November through April of 1979–2016 power spectra of 15°S–15°N, 110°E–140°W averaged OLR anomalies that are (a) unfiltered, (b) filtered for eastward zonal wave numbers, and (c) filtered for westward zonal wave numbers in the black curves. The red noise and 95% confidence spectra are also shown in the red dashed and blue dotted curves, respectively. The gray lines highlight the 15–100-day band.

of this paper is as follows. In section 2, we briefly discuss the data sets used. In section 3, we identify the westward propagating intraseasonal mode and illustrate its physical structure along with that of the MJO. To explain the fundamental differences in zonal propagation between this westward propagating mode and the MJO, a column-integrated MSE budget analysis is computed in section 4. Section 5 discusses the potential of interannual variations of intraseasonal convection activity over the WP associated with both the westward propagating mode and the MJO. Section 6 discusses the potential origins of the westward propagating intraseasonal mode we highlight in this study. A summary and conclusions section wraps up our findings in section 7.

2. Data Sets

Daily estimates of OLR are used in this study as a proxy for deep convection in the tropics (e.g., Figure 1); they are from the National Oceanic and Atmospheric Administration (NOAA) polar-orbiting satellite data set (Liebmann & Smith, 1996). The OLR has been interpolated onto a uniform spatial grid of 2.5° × 2.5° for all latitudes and longitudes and for the years of 1979 through 2016. Two- and three-dimensional (22 standard pressure levels) daily averaged fields from the European Centre for Medium-Range Weather Forecasts (ECMWF) ERA-Interim reanalysis (Dee et al., 2011) are used for analyses of the physical structures associated with the MJO and westward propagating intraseasonal oscillations and budget analyses of the column-integrated MSE. ERA-Interim fields are for the same time period as OLR and are interpolated onto the same horizontal spatial grids as OLR for all latitudes and longitudes. The ERA-Interim reanalysis fields include horizontal winds, vertical pressure velocity, geopotential, temperature, specific humidity, surface latent heat flux, surface sensible heat flux, surface pressure, and surface and top of the atmosphere radiative fluxes. In the following analysis, we focus our analyses on an extended boreal winter season (November through April).

3. Eastward and Westward Propagating Intraseasonal Modes Over the WP

3.1. Extended EOF Analysis of Intraseasonal OLR

Since we focus on intraseasonal variability over the WP that may include aspects of $n = 1$ ER waves, a wide temporal band of 15–100 days is used in this study. This choice is well supported by the power spectrum of OLR anomalies (with seasonal cycle and first three annual harmonics removed) averaged over the tropical western and central Pacific (15°S–15°N, 110°E–140°W), which is shown in Figure 2a. Also displayed in Figures 2b and 2c are the power spectra for only eastward and only westward zonal wave numbers, respectively. There is one main intraseasonal spectral peak centered near 45 days in the full spectrum and the spectrum for eastward propagating wave numbers (Figures 2a and 2b). These peaks are above the red noise and 95% confidence spectra (Gilman et al., 1963) and are mainly attributable to the MJO. For westward wave numbers (Figure 2c), there are two spectral peaks centered near 20 and 30 days, likely related to the westward propagating disturbances observed in Figures 1c and 1f. This result serves as motivation to not use a narrower frequency band-pass filter on OLR than 15–100 days since narrower bands may lead to aliasing of the 20-day peak in westward propagating OLR variance.

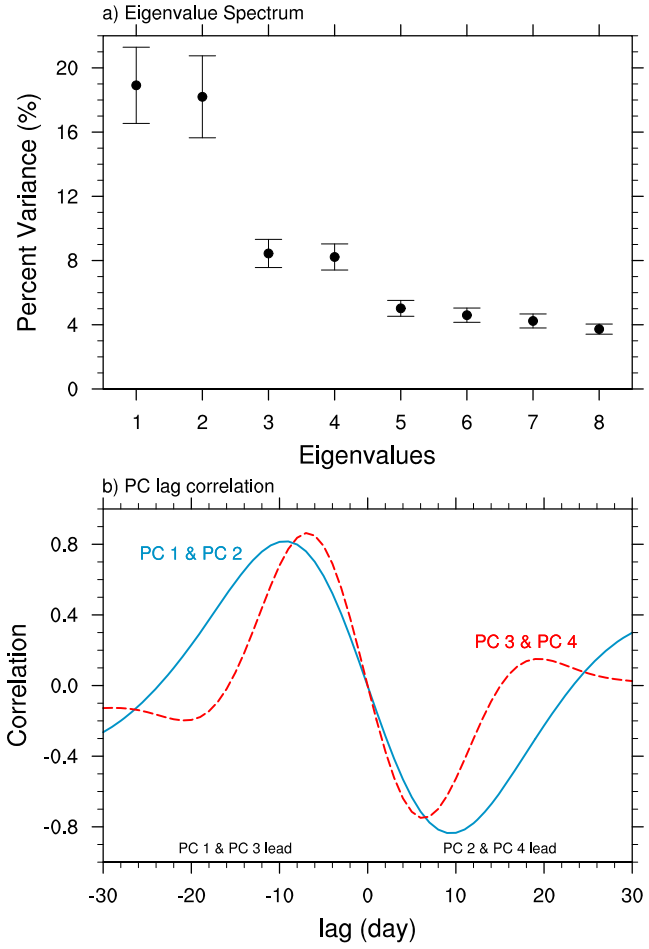

Figure 3. (a) Percent variance explained by the eight leading eigenvalues with bars that represent eigenvalue sample error and (b) correlation between the first two pairs of PCs as a function of daily lag (e.g., positive values mean that PC 2 leads PC 1 and PC 4 leads PC 3).

To identify the dominant intraseasonal variability modes over the WP as motivated by Figure 1, we perform an extended EOF (EEOF) analysis (Weare & Nasstrom, 1982) of 10°S–10°N averaged 15–100-day band-pass-filtered OLR anomalies over 110°E–140°W using 21 temporal lags for November through April 1979–2016 (at lag = 0). For example, lag = −10 days corresponds to 22 October through 20 April, lag = 0 days to 1 November through 30 April, and lag = 10 days to 11 November through 10 May. The OLR anomalies are first subjected to the removal of their seasonal cycle, and the first three harmonics before a 15–100-day Lanczos band-pass filter (Duchon, 1979) is applied using 201 points. Note that the results from the EEOF analysis are somewhat sensitive to the number of temporal lags; similar results can be obtained with lags greater than about 15 days, with smaller lags leading to more spread out eigenvalues (in percent variance explained) and thus less coherent propagating modes (the limiting case of zero lags is the same as a standard EOF analysis). Since we are concerned with comparing eastward and westward propagation of intraseasonal convection along the equator, the intraseasonal OLR is averaged from 10°S to 10°N and the EEOF analysis is conducted over the longitudes 110°E–140°W; these are regions with prominent variability in both eastward and westward equatorial OLR propagation based on longitude-lag diagrams such as those in Figure 1. Slight shifting of these regions, such as averaging intraseasonal OLR over 15°S to 15°N or analyzing the longitudes 120°E–160°W, leads to very similar results.

The main features of the EEOF analysis are conveyed in Figure 3, with the percentage of variance explained by the leading eight eigenvalues shown in Figure 3a and the lag correlation between the two leading pairs of normalized principal components (PCs) shown in Figure 3b. In Figure 3a, the error bars represent the sampling error ranges estimated following North et al. (1982), with effective sample size estimated based on autocorrelations of each PC (Bretherton et al., 1999). As can be seen from Figure 3 a, the first two pairs of eigenvalues are well separated from other eigenvalues. According to Figure 3a, the first and second pairs of eigenvalues explain approximately 37 and 17% of the total OLR variance, respectively. Meanwhile, PC 1 and PC 2 have peak correlations of 0.82 and −0.83 at lags of −9 and 9 days, respectively, and PC 3 and PC 4 have peak correlations of 0.86 and −0.75 at lags of −7 and 6 days, respectively, suggesting a period of approximately 40 days for the first leading EEOF mode and 25 days for the secondary EEOF mode.

3.2. Horizontal Structure of the Leading WP Intraseasonal Modes

Lag regressions onto PC 1 of the unfiltered OLR and unfiltered 850-hPa wind anomalies are illustrated in Figures 4a–4g, representing the well-documented eastward propagating MJO, with a zonal wave number of 2–3 and with convection initiating in the Indian Ocean and propagating eastward at 4–5 m/s until just east of the Dateline. Two off-equatorial cyclonic gyres and equatorial westerlies are discerned to the west of enhanced convection, while equatorial easterlies are evident to the east of enhanced convection. These large-scale features roughly resemble the atmospheric response to a stationary (e.g., Gill, 1980) or eastward propagating diabatic heating (Schubert & Masarik, 2006). For the rest of this study, we refer to this first leading intraseasonal mode identified by the EEOF analysis of OLR over the WP as the MJO. If otherwise not stated, all projections or regressions are onto normalized PC 1 for this mode.

In Figures 4h–4n, the time evolution and horizontal structure of unfiltered OLR and unfiltered 850-hPa wind anomalies of the second mode of the EEOF analysis are shown via lag regressions onto PC 4. It is a wave number 3–4 disturbance, with convection initiating near 10°S just east of the Dateline and propagating west-northwestward at about 5 m/s over the central and WP and significantly weakening near the Philippines at lag = 15 days. We refer to this second prevailing intraseasonal mode as the westward

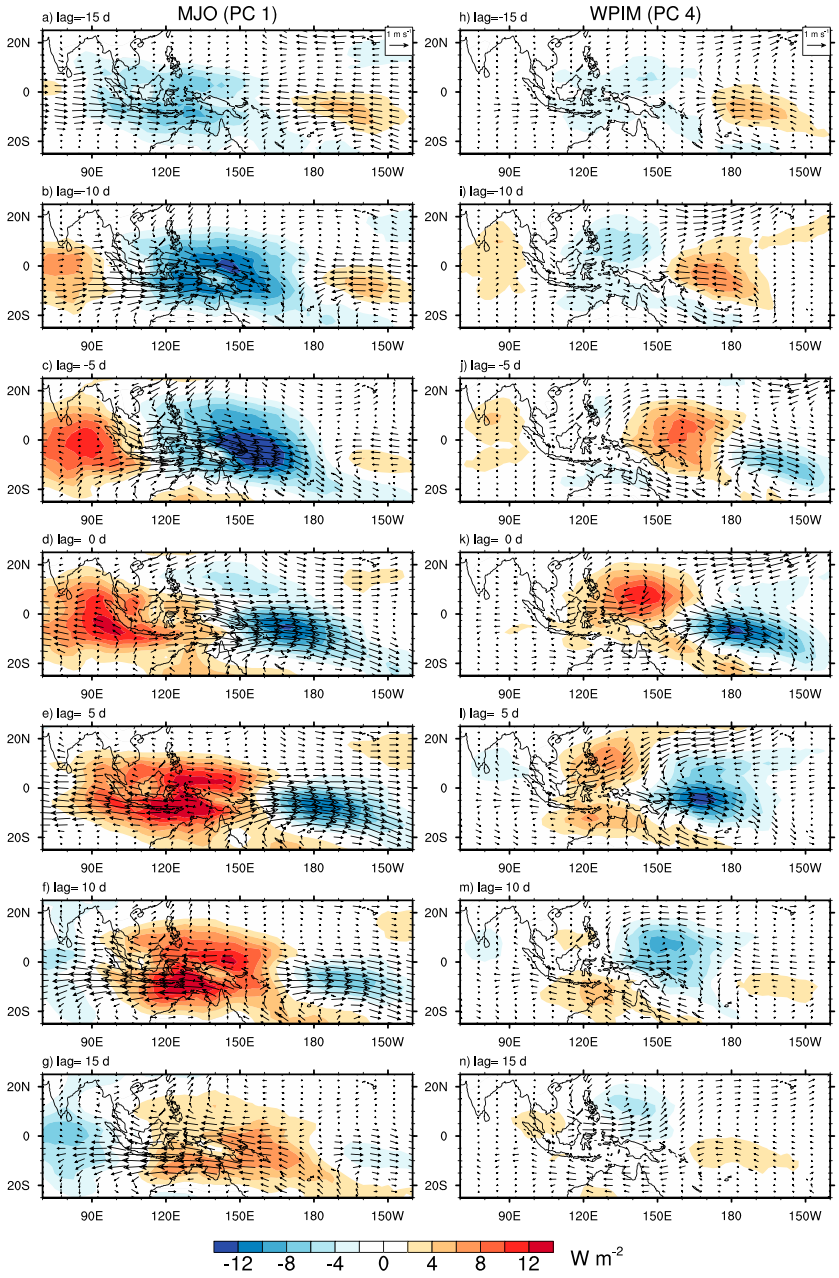

Figure 4. Unfiltered anomalies of OLR (shading) and 850-hPa horizontal wind (vectors) lag regressed onto PC 1 (left panels, MJO) and PC 4 (right panels, WPIM). The PCs are normalized and the lag regressions are multiplied by −1 standard deviation of the PCs.

propagating intraseasonal mode (WPIM). All subsequent projections or regressions for the WPIM are onto normalized PC 4. There are strong low-level equatorial westerlies surrounded by a pair of off-equatorial cyclonic gyres near and west of the enhanced convection, particularly from lag = 0 days to lag = 10 days. Note that the WPIM gyres are smaller in horizontal scale than those associated with the MJO. In the region of suppressed convection farther west, there is a pair of off-equatorial anticyclonic gyres. As the WPIM propagates west-northwestward, the northern cyclonic gyre strengthens, while the southern cyclonic gyre dissipates, exerting a greater impact on the Philippine Sea and northern part of the Maritime Continent rather than northern Australia.

It has been shown for $n = 1$ ER waves that westward propagating extratropical dry disturbances form in the eastern Pacific before convection couples to their circulation closer to the equator (e.g., Kiladis & Wheeler,

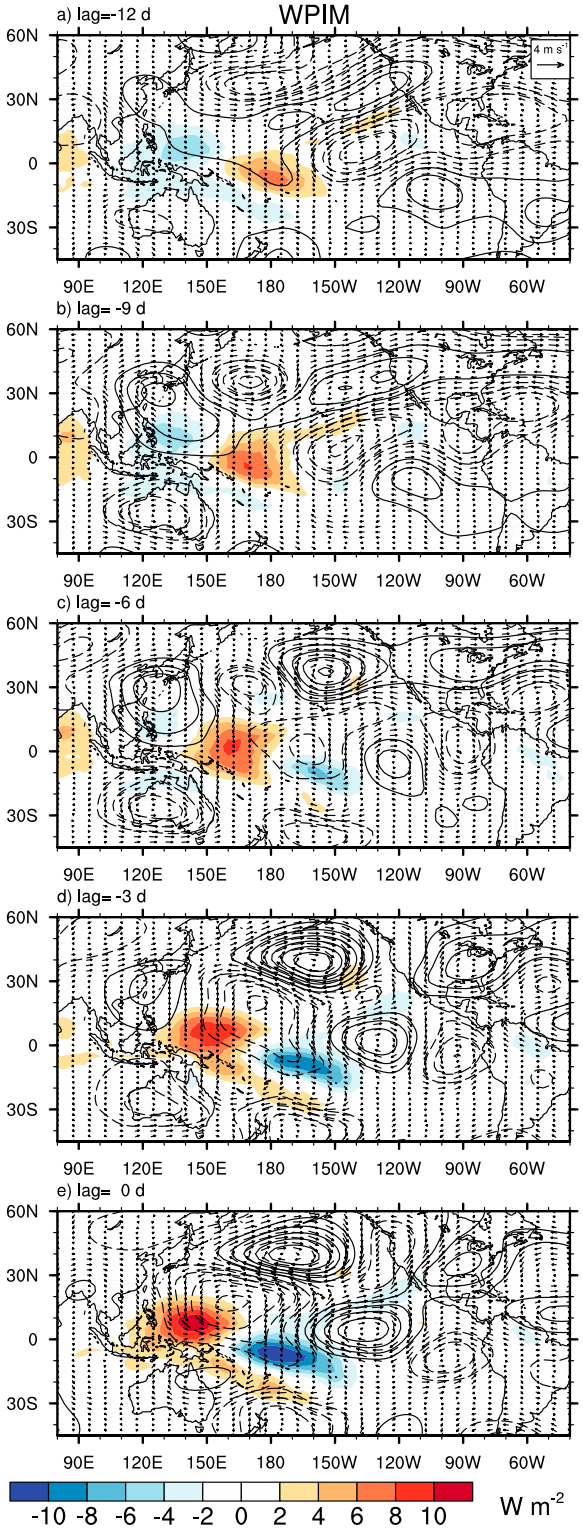

Figure 5. Unfiltered anomalies of OLR (shading), 200-hPa stream function (contour lines), and 200-hPa horizontal wind (vectors) lag regressed onto PC 4 showing the influence of extratropical waves preceding lag = 0. The PCs are normalized, and the lag regressions are multiplied by −1 standard deviation of the PCs. The stream function contour lines are from −2 to 3 m^2/s every 0.5 m^2/s with the zero line omitted.

1995; Kiladis, 1998; Numaguti, 1995; Pires et al., 1997). Thus, we have investigated if there are dry westward propagating disturbances that precede the initiation of the WPIM near the Dateline by analyzing the time evolution of unfiltered anomalies of OLR, 200-hPa stream function, and 200-hPa horizontal winds over a relatively wide domain in Figure 5. There is a clear influence of extratropical disturbances days before the WPIM intensifies over the central Pacific Ocean, including a northwest to southeast oriented wave train in upper level winds and stream function over the Pacific Ocean. The alternating upper level troughs and ridges also have a northeast to southwest tilt, mainly at lags −9 and −12, which is characteristic of similar extratropical to cross-equatorial wave trains observed in Kiladis (1998). As the WPIM intensifies from lag −6 to lag 0, the alternating upper level troughs and ridges intensify and become more like closed lows and highs propagating mainly westward. Subsequent upper level wave development to the southeast appears to be present; however, this is more difficult to discern.

Note that we have also performed our EEOF analysis of 15–100-day filtered OLR over the Indian Ocean region (50° to 160°E). While the MJO is captured in the first two EEOFs in this case, a coherent westward propagating mode is absent in the EEOF analyses over the Indian Ocean (figure not shown). This is in general agreement with Figure 1 and for the intraseasonal convective propagation during many other winter seasons. That is, westward propagating intraseasonal disturbances tend to weaken significantly over or near the Maritime Continent before reaching the Indian Ocean.

3.3. Vertical Structure of the Leading WP Intraseasonal Modes

Next, the vertical structure of the WPIM is further examined and compared to that of the MJO. Figure 6 illustrates 15°S–5°N averaged unfiltered anomalies of specific humidity, zonal wind, and vertical pressure-velocity via regressions onto PC 1 (MJO, left) and PC 4 (WPIM, right). The vertical gray lines in each plot represent the corresponding longitudes of the minimum OLR anomalies. The cross sections of specific humidity and vertical velocity anomalies of the MJO in Figures 6a and 6c illustrate the well-known westward tilt with height associated with the MJO (Jiang et al., 2011; Jiang et al., 2015; Kiladis et al., 2005; Tian et al., 2010). The anomalous zonal wind also exhibits the typical characteristics of the MJO in the WP, that is, a first baroclinic vertical structure, with strong low-level westerlies below upper level easterlies mainly to the west of the convective center (Figure 6b).

In contrast to the MJO, the vertical structure of specific humidity anomalies for the WPIM shows rather weak vertical tilting (Figure 6d). The zonal wind anomalies in Figure 6e illustrate a nearly barotropic vertical structure with responses mainly near and to the west of the convective center, with strong low-level westerlies extending to 300 hPa and very weak easterly wind anomalies above 150 hPa. In the suppressed region near 150°E, there are weak low-level easterlies below strong upper level westerlies (Figure 6e), which is more indicative of a first baroclinic mode vertical structure. The vertical velocity structure of the WPIM (Figure 6f) does show slight westward tilt with height like the MJO, although the tilting is weaker than the MJO and the region of rising motion is narrower in longitude. Considering that the WPIM propagates westward, the results in Figure 6 suggest that the backward tilt with height in anomalous moisture and vertical velocity fields observed for the MJO is not clearly evident for the WPIM. The WPIM vertical structures are quite similar to those

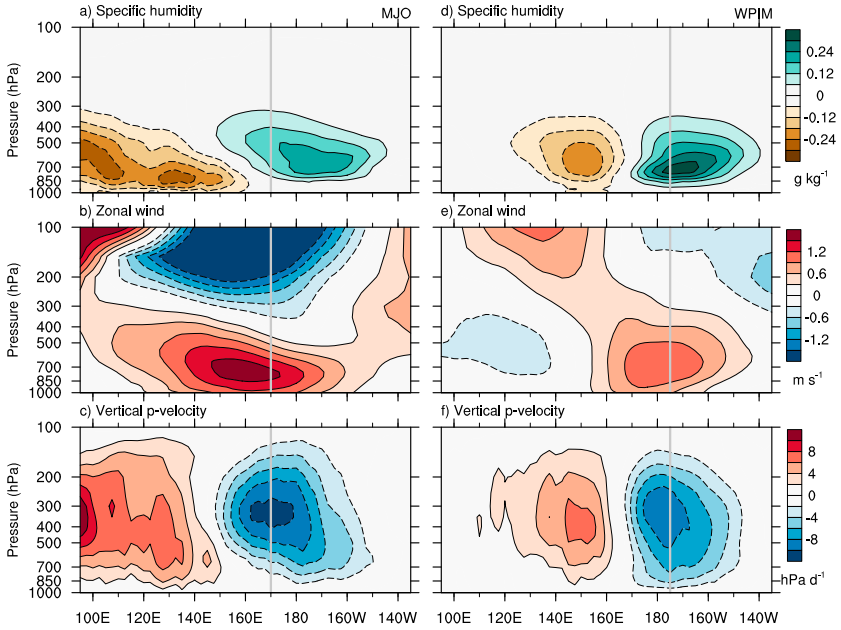

Figure 6. Longitude-pressure unfiltered anomalies of specific humidity, zonal wind, and vertical pressure velocity averaged over 15°S–5°N and regressed onto (a–c) PC 1 (left, MJO) and (d–f) PC 4 (right, WPIM). The PCs are normalized, and the longitude of the OLR minima for each mode is denoted by the vertical grey lines.

presented for $n = 1$ ER waves by Kiladis et al. (2009), with the idea that as these disturbances propagate from the central to WP (approach the Indo-Pacific warm pool), their vertical structure becomes less barotropic and more like the first baroclinic mode (Mapes et al., 2006).

4. Budget Analysis of the Column-Integrated MSE Equation

Evaluating the column-integrated MSE equation has provided critical insights to mechanisms associated with the MJO propagation (e.g., Adames & Kim, 2016; Andersen & Kuang, 2012; Inoue & Back, 2015; Jiang, 2017; Kim et al., 2014; Maloney, 2009; Pritchard & Bretherton, 2014; Sobel et al., 2014; Sobel et al., 2001). The underlying basis of this approach is that the MJO is considered to be a "moisture mode," wherein MJO precipitation is mainly controlled by atmospheric column moisture. If weak temperature gradient balance holds, column-integrated MSE perturbations are mainly attributed to variations in atmospheric moisture, and thus column-integrated MSE can be a proxy for MJO convection.

Moisture mode theory is also appropriate for studying phenomena such as the WPIM since it lies in a region of spectral space where weak temperature gradient balance holds (Wolding et al., 2016). From Figure 24 in Wolding et al. (2016), it appears that the time and space scales where this balance should hold best is at intraseasonal timescales (approximately 15-day periods or greater) and large zonal wave numbers (approximately zonal wave number 6 or smaller) for both eastward and westward propagating wave numbers. The MJO falls within this spectral space and so does the WPIM; thus, we proceed with a budget analysis of column-integrated MSE to identify key processes in regulating the different propagation features between the MJO and WPIM.

The column-integrated MSE equation is given by

$$\left\langle \frac{\partial h}{\partial t} \right\rangle = -\langle \vec{v} \cdot \nabla h \rangle - \left\langle \omega \frac{\partial h}{\partial p} \right\rangle + \langle Q_R \rangle + F_S, \tag{1}$$

where h is the MSE, $\vec{\boldsymbol{v}} = (u, v)$ is the horizontal (zonal, meridional) winds, ω is the vertical pressure-velocity, F_S represents the sum of surface latent and sensible heat fluxes, and $\langle Q_R \rangle$ is the column-integrated radiative heating. The brackets represent the mass-weighted vertical integral from the surface (using surface pressure) to 150 hPa. Note that the vertical structure of radiative heating is not available for an explicit calculation of

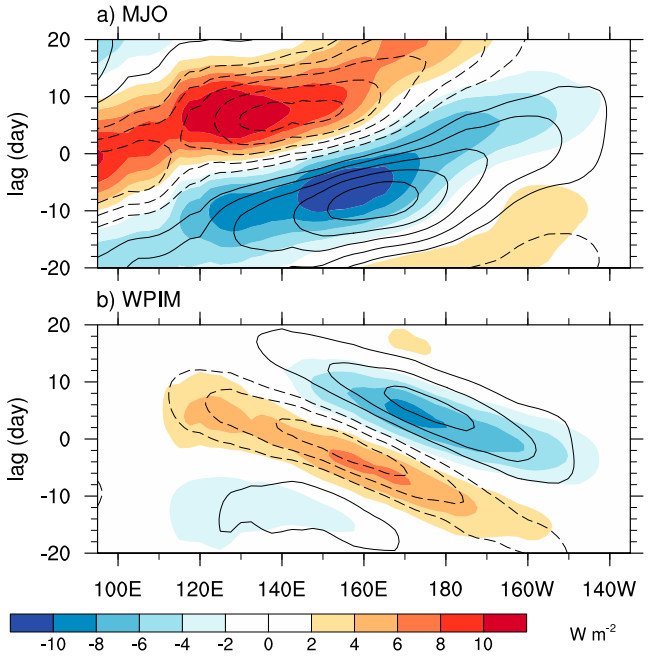

Figure 7. Longitude-lag anomalies of 15°S–5°N averaged unfiltered OLR (shading) and unfiltered column-integrated MSE (contour lines) lag regressed onto (a) PC 1 (normalized, MJO) and (b) PC 4 (normalized, WPIM). For the MSE isolines, the contour interval is 1×10^6 J/m^2, negative values are dashed and the zero line is omitted.

$\langle Q_R \rangle$ based on the ERA-Interim reanalysis; $\langle Q_R \rangle$ is estimated using the fluxes at the surface and top of the atmosphere (e.g., Kim et al., 2014).

As demonstrated in Figure 7, which shows 15°S–5°N averaged unfiltered OLR and unfiltered column-integrated MSE anomalies lag regressed onto PC 1 (MJO) and PC 4 (WPIM), column-integrated MSE anomalies are highly anticorrelated with OLR anomalies for both of these intraseasonal modes, with a lag versus longitude pattern correlation of −0.83 and −0.85 for the MJO and WPIM, respectively, in accord with moisture mode theory. For the MJO, the maximum anticorrelation (−0.99) in longitude between OLR and column-integrated MSE occurs when MSE leads by 3 days. For the WPIM, the maximum anticorrelation (−0.97) in longitude occurs when OLR leads by 2 days—this is a caveat to the WPIM, implying that there is an export of column MSE (rather than an MSE import into the column as it is for the MJO) before peak convection occurs. One possible explanation for this caveat has to do with a nonnegligible residual in the column-integrated MSE budget, which is shown explicitly in Figures 9 and 10.

To explore fundamental processes responsible for the distinct propagation features of the MJO and WPIM, Figure 8 illustrates the horizontal structure of the unfiltered anomalies of column-integrated MSE tendency, horizontal and vertical MSE advection, radiative fluxes, surface (latent and sensible) heat fluxes, and the residual regressed onto PC 1 (MJO, left) and PC 4 (WPIM, right). Positive unfiltered column-integrated MSE anomaly values greater than or equal to 2.0×10^6 J/m^2 are overlaid in the black dotted contours. Note that the latitude ranges for the two modes are slightly different but they are the same size (30° latitude by 60° longitude); the regions are approximately centered about each mode's column-integrated MSE maxima. For the MJO, the column-integrated MSE maxima are located at 15°S, 180°, whereas for the WPIM, the column-integrated MSE maxima are centered near 5°S, 175°W. The MSE tendency for the MJO shows negative values to the west and positive values to the east of the MSE center (Figure 8a), implying eastward MSE propagation. For the WPIM, the opposite structure exists, with positive MSE tendencies to the west and negative MSE tendencies to the east of the MSE center (Figure 8e), which is consistent with its westward propagation (see Figures 4h–4n).

The spatial pattern of column-integrated horizontal MSE advection for the MJO (Figure 8b) is largely similar to the pattern of MSE tendency, lending further support of the important role of horizontal MSE advection for MJO propagation (e.g., Jiang, 2017; Kim et al., 2014; Kim et al., 2017; Maloney, 2009). For the WPIM, the horizontal MSE advection pattern (Figure 8h) also strongly resembles the total MSE tendency pattern with the largest positive MSE tendencies mainly to the west-northwest of the MSE center in addition to having small negative MSE tendencies to the east. These results indicate that similar to the MJO, horizontal MSE advection also plays a critical role in the westward propagation of the WPIM.

The vertical MSE advection and radiative flux patterns associated with both modes are largely anticorrelated and shifted slightly west (northwest for MJO, southwest for WPIM) of their MSE centers, as seen from Figures 8c, 8d, 8i, and 8j. These structures support the idea that vertical MSE advection acts to export MSE through convection-induced vertical motion as described in previous studies (e.g., Andersen & Kuang, 2012; Jiang, 2017; Jiang et al., 2016; Kim et al., 2014). On the other hand, radiative fluxes, particularly the longwave component (not shown), have a destabilizing effect associated with reduced longwave cooling that is shifted slightly west of the convective center (e.g., Andersen & Kuang, 2012; Jiang, 2017; Raymond, 2001; Sobel et al., 2014).

As for surface heat fluxes, which is the sum of sensible and latent heat fluxes, they have positive tendencies that are also shifted to the west of the MJO MSE center (Figure 8e), with the main contribution from the latent heat flux (not shown), wherein enhanced wind speeds due to anomalous surface westerlies to the west of the MSE center constructively interfere with background westerly surface winds. Therefore, radiative and

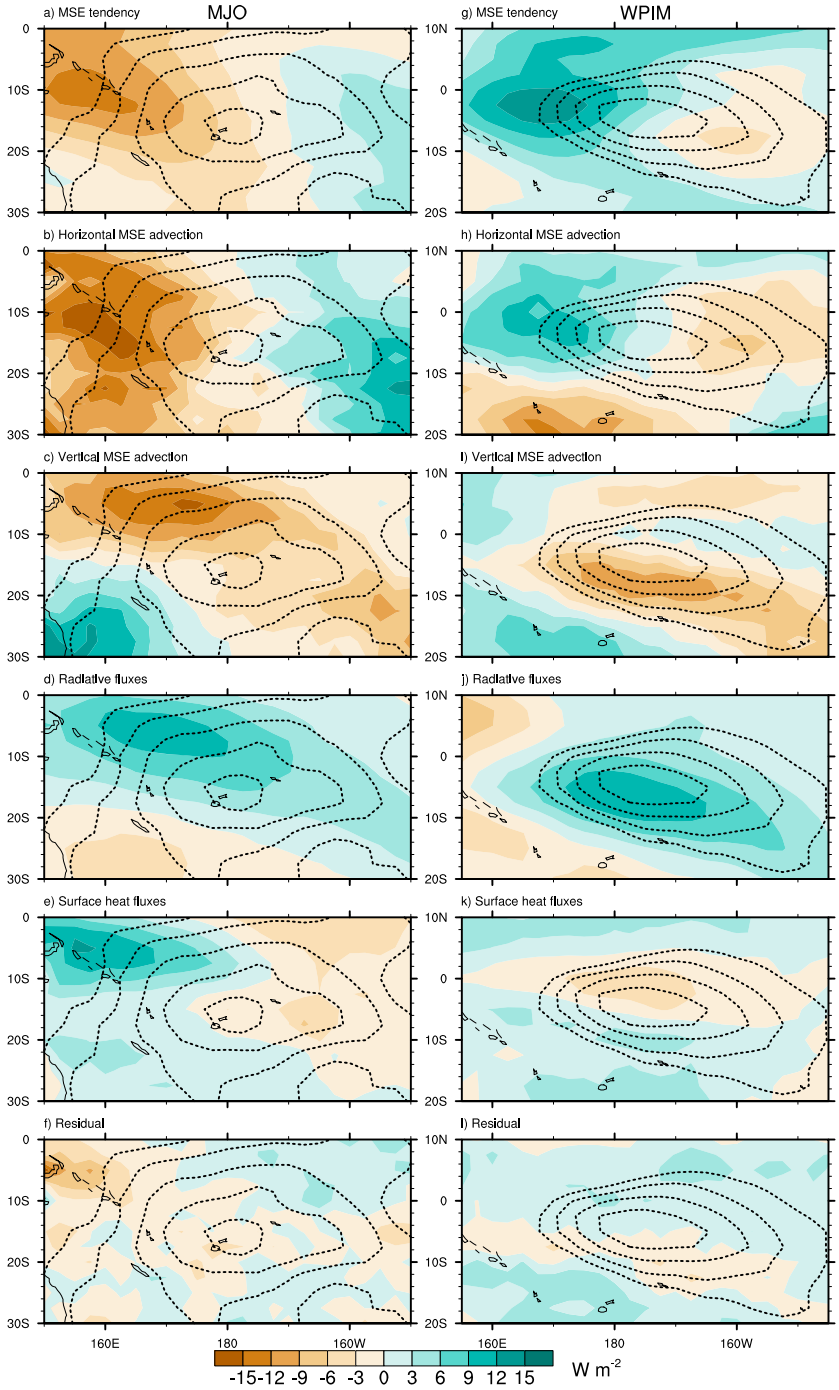

Figure 8. Regressions of the unfiltered anomalous column-integrated MSE budget terms (shading) and column-integrated MSE (dotted contour lines) onto (a–f) PC 1 (normalized, MJO) and (g-l) PC 4 (normalized, WPIM). For the column-integrated MSE anomalies, only values greater than or equal to 2×10^6 J/m^2 are plotted (contour interval of 1×10^6 J/m^2).

surface heat fluxes do not contribute to the MJO's eastward propagation (Jiang, 2017; Kim et al., 2014; Maloney, 2009).

The surface heat flux pattern of the WPIM (Figure 8k) is characterized by small positive MSE tendencies south of the MSE center and small negative tendencies to the north (where anomalous westerlies

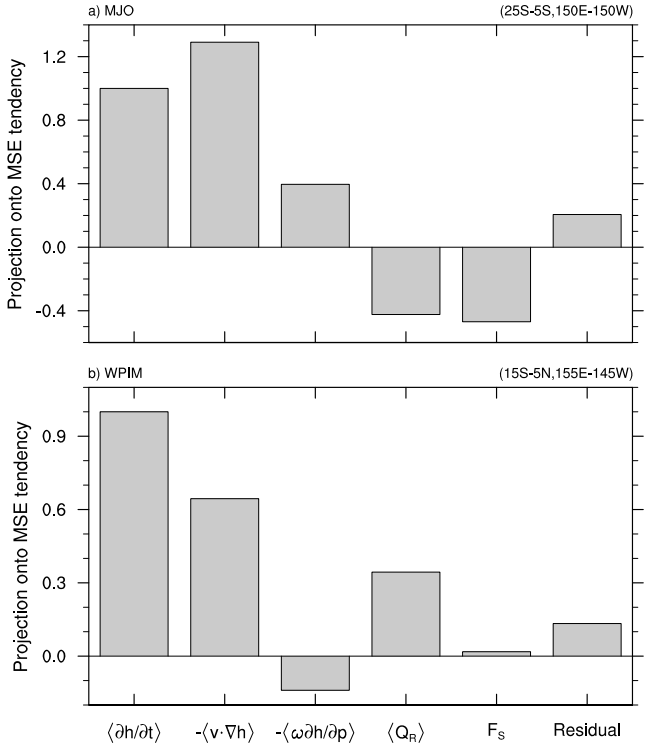

Figure 9. Area-weighted horizontal projections of the anomalous column-integrated MSE terms from Figure 8 (and their residual) onto the MJO and WPIM column-integrated MSE tendency anomalies over the regions (a) 25°S–5°S, 150°E–150°W (MJO) and (b) 15°S–5°N, 155°E–145°W (WPIM). Positive projection coefficients correspond to eastward and westward propagation the MJO and the WPIM, respectively.

destructively interfere with background easterlies). There is very little zonal asymmetry in the surface flux pattern; therefore, it does not contribute to zonal propagation of the WPIM.

To more objectively quantify the relative contributions of each MSE term to the total MSE tendency, the spatial pattern of each budget term is projected onto the total MSE tendency pattern for both the MJO and WPIM (i.e., Figures 8a and 8g), illustrated in Figure 9. For these projections, the regression corresponding to each column-integrated MSE budget term is multiplied by the regression of the column-integrated MSE tendency (this product is area weighted) and then divided by the area-weighted square of the column-integrated MSE tendency (e.g., Andersen & Kuang, 2012). Positive projections correspond to eastward and westward propagation the MJO and the WPIM, respectively. This can be explained by the spatial structure of the column-integrated MSE tendency in Figures 8a and 8g. The MSE budgets for both modes have small residuals, which lends confidence to our conclusions. Note that the MSE budget residual for the MJO has been discussed previously (e.g., Jiang, 2017; Kiranmayi & Maloney, 2011; Mapes & Bacmeister, 2012). The MSE budget residuals for both modes indicate that there is a missing moistening source in advance of intraseasonal convection, which may partially explain the export of MSE that occurs before the peak in WPIM convection (Figure 7b).

Consistent with the discussions of Figure 8 and what has been stated in many previous studies, the leading term associated with the total MSE tendency of the MJO, thus largely responsible for its eastward propagation, is the horizontal MSE advection. Vertical MSE advection also yields a positive projection over the WP, but it is much smaller than the horizontal MSE advection projection. As expected, both the radiative and surface heat fluxes yield negative projections, indicative of an inhibition of eastward propagation of the MJO.

The total MSE tendency associated with the WPIM, which helps explain its westward propagation, is regulated primarily by horizontal MSE advection and has a smaller contribution from radiative fluxes (projection coefficients of 0.64 and 0.34, respectively). Vertical MSE advection promotes eastward propagation and thus inhibits the westward propagation of the WPIM (negative projection). Meanwhile, surface fluxes have a near-zero projection coefficient for the WPIM indicating that they do not promote horizontal propagation of the WPIM.

Since radiative heating plays a similar role for both the MJO and WPIM by inducing a slight westward propagation of intraseasonal convection, possibly due to a similar vertically westward tilting structures in both of these two modes (Figures 6c and 6f), a key process responsible for the distinct propagation features between the MJO and WPIM is the horizontal MSE advection. For the MJO, the horizontal MSE advection generates moistening to the east and drying to the west of the convection, promoting the eastward propagation of the MJO by offsetting the inhibition by the radiative effect and surface fluxes. For the WPIM, the horizontal MSE advection produces moistening to the west and drying to the east of convection, thus promoting westward propagation of the WPIM (along with nonnegligible contributions by radiative fluxes).

In order to understand differences in horizontal MSE advection between the MJO and WPIM, we further investigate the horizontal MSE advection term by decomposing the horizontal winds and MSE into three different timescales: low frequency (>100 days, with the seasonal cycle and first three harmonics retained), intraseasonal (15–100 days, with the seasonal cycle and first three harmonics removed), and high frequency (2–15 days, with the seasonal cycle and first three harmonics removed). Figure 10 displays projection coefficients of the (unfiltered) total column-integrated horizontal MSE advection anomalies and the nine terms associated with the decomposition of horizontal MSE advection along with residuals onto the MSE tendency anomalies for the MJO and WPIM. Note the mathematical notation used, for example, $h = \underline{h} + h' + h^*$,

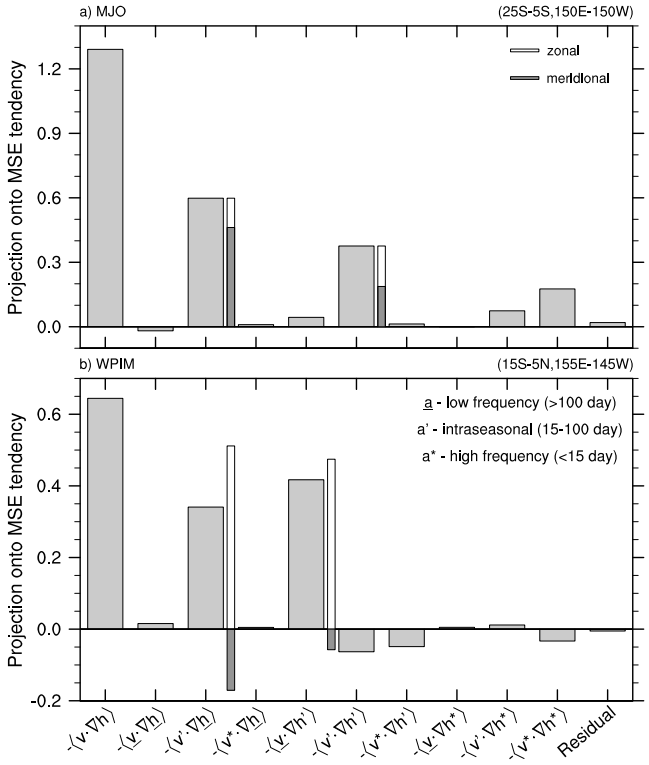

Figure 10. Area-weighted horizontal projections of temporally decomposed column-integrated anomalous horizontal MSE advective terms onto the column-integrated anomalous MSE tendency over the regions (a) 25°S–5°S, 150°E–150°W (MJO) and (b) 15°S–5°N, 155°E–145°W (WPIM). Zonal and meridional components of the leading terms for the MJO and WPIM are also shown.

where $\underline{h}$ represents the low-frequency component, h' the intraseasonal component, and h^* the high-frequency component. Also plotted are the zonal and meridional components for the leading horizontal advection terms for each mode in the thin white and dark gray histograms, respectively.

For the MJO, the leading term associated with eastward propagation from the decomposition is the horizontal advection of the low-frequency MSE by the intraseasonal winds, $-\overrightarrow{\boldsymbol{v}'}\cdot\nabla\underline{h}$, in general agreement with MJO propagation over the Indian Ocean (e.g., Benedict et al., 2015; Jiang, 2017; Kim et al., 2014). Both the zonal and meridional components of this term have positive projections with the meridional term being more critical over the WP. Additionally, the MSE advection by intraseasonal eddies term, $-\overrightarrow{\boldsymbol{v}'}\cdot\nabla h'$ (and to a lesser degree $-\overrightarrow{\boldsymbol{v}^*}\cdot\nabla h^*$) also contributes to the total horizontal advection for the MJO. Further analysis of this $-\overrightarrow{\boldsymbol{v}'}\cdot\nabla h'$ indicates that these eddies are mainly at timescales less than 25 days (not shown), making them similar to synoptic eddies seen in many previous studies on MJO propagation over the WP (e.g., Kiranmayi & Maloney, 2011; Maloney, 2009).

For the WPIM, the most dominant term contributing to its westward propagation is the horizontal advection of the intraseasonal MSE anomalies by the low-frequency winds, $-\overrightarrow{\underline{\boldsymbol{v}}}\cdot\nabla h'$. The zonal component of this term is particularly crucial to westward propagation, while the meridional component acts as an inhibitor of westward propagation. There is also a term of secondary importance, the horizontal advection of the low-frequency MSE by the intraseasonal winds, $-\overrightarrow{\boldsymbol{v}'}\cdot\nabla\underline{h}$. Similar to $-\overrightarrow{\underline{\boldsymbol{v}}}\cdot\nabla h'$, the zonal component of this term dominates the meridional counterpart for the westward propagation of the WPIM.

These above results suggest that the distinct propagation characteristics between the MJO and WPIM are likely associated with either differences in their intraseasonal circulations or changes in their background mean state, such as zonal winds and MSE. Since the horizontal MSE advection driving the propagation of the MJO and the WPIM is mainly confined to the lower troposphere (not shown), and considering that patterns for low-level MSE are very similar to those for low-level specific humidity, we further investigate interannual variations in low-level zonal wind and specific humidity over the WP.

5. Interannual Variability Over the WP

Variations in the background mean low-level specific humidity and low-level zonal winds may play a significant role in determining the propagation characteristics of intraseasonal convection over the WP. In this section, we perform further analyses on interannual variations of intraseasonally propagating convective events over the WP as motivated in section 1. We first provide a basis for performing such analyses by producing indices that rank interannual eastward and westward OLR propagation over the WP.

For this analysis, time-longitude Hovmöller diagrams of OLR anomalies associated with the MJO and WPIM are first derived by performing lag regressions of 15–100-day band-pass-filtered OLR anomalies for all winters from 1979 to 2016 onto two OLR time series from the EEOF analysis, one corresponding to the MJO and the other corresponding to the WPIM. The two OLR time series are based on OLR that has been reconstructed by each mode's PCs and EEOFs for temporal lag = 0 (1 November through 30 April) and averaged over the WP (165°E–175°E). For example, for the MJO we reconstruct the OLR using PC1*EEOF1(lag = 0) + PC2*EEOF2(lag = 0). Recall that EEOF analysis was performed on 15–100-day OLR anomalies averaged over 10°S–10°N; therefore, OLR anomalies are only a function of time and longitude when they are reconstructed. The resulting time-longitude Hovmöller diagrams for the MJO and the WPIM are shown in Figures 11a and 11b.

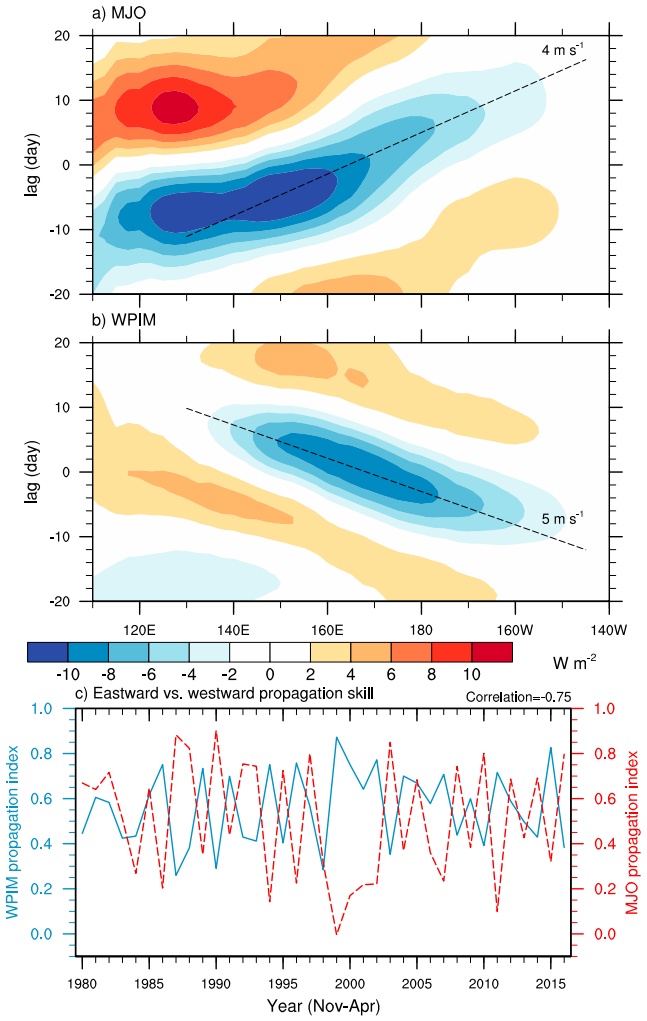

Figure 11. 10°S–10°N averaged 15–100-day band-pass-filtered OLR anomalies lag regressed onto reconstructed OLR anomalies for the (a) MJO and (b) WPIM and averaged over 165°–175°E. (c) MJO propagation index (red dashed curve) and WPIM propagation index (blue solid curve) for each winter season. The indices are computed by pattern correlations over the tropical WP between each season's longitude-lag diagram of intraseasonal OLR and the longitude-lag diagrams for the MJO and WPIM in (a) and (b), respectively. The correlation coefficient (−0.75) between the two indices is shown in the top right.

Meanwhile, zonal propagation of intraseasonal convection over the tropical WP for each winter from 1979 to 2016 can be similarly obtained by Hovmöller diagrams based on 15–100-day band-pass-filtered OLR anomalies lag regressed onto their averaged values over 5°S–5°N, 165°E–175°E for each corresponding winter. Then two propagation indices are computed for each winter that represent the main propagation characteristics of the MJO and WPIM, by pattern correlations of the time-longitude OLR Hovmöller diagram during that particular winter against that of the MJO and WPIM. These indices are referred to as the MJO and WPIM propagation indices.

Figure 11c illustrates year-to-year variations of the MJO (red) and WPIM (blue) propagation indices for 1980 to 2016 winter seasons. Significant interannual variations in both indices are readily seen. Particularly, a substantial anticorrelation (−0.75) between these two indices is noted, suggesting that during winters when the eastward propagating MJO is active, the WPIM tends to be damped, and vice versa. Two groups of years, namely, years characterized by strong eastward and westward propagation, can be identified by the top either nine (or 10) values of their respective indices (approximately the top 25%). Note that there are no overlaps between these nine (or 10) strong eastward and westward propagation years. These two groups can then be used to perform composite analyses on a number of other fields/features, such as the background state and convectively coupled equatorial waves.

We proceed by comparing the winter mean patterns of the low-frequency (>100-day timescales) low-level zonal winds and low-level specific humidity associated with strong MJO propagation years and strong WPIM propagation years. Figure 12 displays the winter mean 600–900-hPa averaged zonal winds for strong MJO propagation years and strong WPIM propagation years and the winter mean 600–900-hPa averaged specific humidity for strong MJO propagation years and strong WPIM propagation years in the top four panels. Additionally, the differences between the composites for zonal wind and specific humidity are shown in the bottom two panels (with climatology overlaid in gray contour lines). Note that the stippling in bottom panels represents locations where statistical significance at the 1% significance level is achieved using the method outlined in Wilks (2016). This method is quite conservative as it takes spatial autocorrelation into consideration by controlling the false discovery rate (Benjamini & Hochberg, 1995), the rate at which the null hypothesis is erroneously rejected.

The largest differences in the low-level mean zonal winds during strong WPIM and MJO activity are found in the equatorial WP and near the Dateline, where there is a significant enhancement of low-level easterlies during strong WPIM years. These anomalously strong mean easterlies could promote the westward propagation of the WPIM through advection of intraseasonal MSE anomalies (see Figures 9b and 10b). It is possible that the northwestward propagation of the WPIM when it reaches the Maritime Continent is guided in part by the anomalous easterlies and the strong climatological easterlies (Figure 12c) extending from the southeast to the northwest through the Philippines.

Meanwhile, differences in low-level mean specific humidity between strong WPIM and MJO years are characterized by dry anomalies near the Dateline and moistening over off-equatorial regions over the Maritime Continent on both sides of the equator during active WPIM or inactive MJO years. This configuration in anomalous mean moisture pattern effectively reduces the meridional gradient of low-level mean moisture over the Maritime Continent region and enhances the westward zonal gradient of mean moisture over the

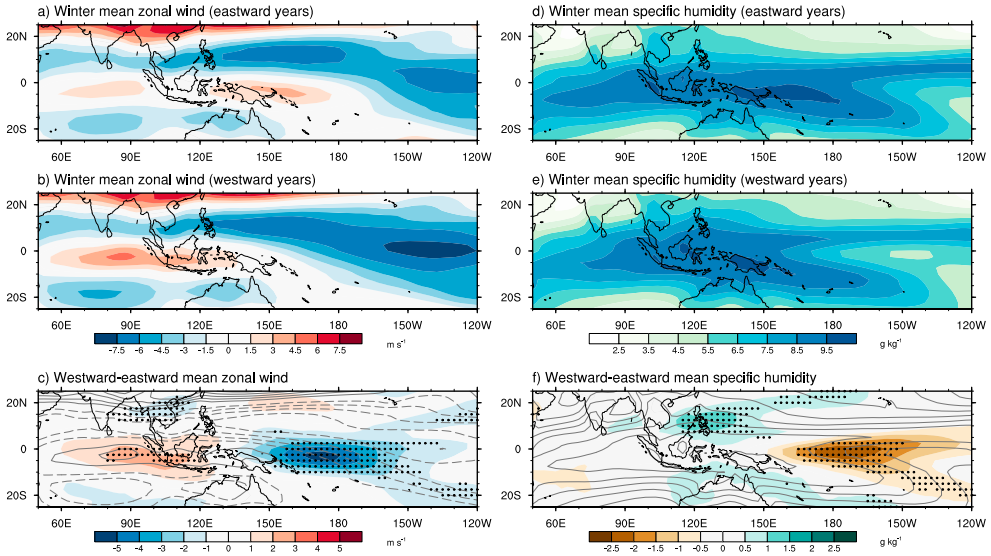

Figure 12. (a) Nine-year composites of low-frequency winter mean specific humidity and zonal wind averaged from 600 to 900 hPa for (a, d) strong MJO years and (b, e) strong WPIM years. Difference in mean 600–900-hPa specific humidity and zonal wind for strong WPIM years minus strong MJO years (shading) and climatology for both fields (gray contour lines). For the climatological zonal wind, the contour lines are from −7.5 to 3.0 m/s, the contour interval is 1.5 m/s, the zero line is omitted, and negative isolines are dashed. For the climatological specific humidity, the contour lines are from 2.5 to 9.5 g/kg every 1 g/kg. Locations where the differences are statistically significant at the 1% significance level are highlighted by black dots.

WP to the east of the Maritime Continent. These features significantly weaken MJO eastward propagation into the WP through both zonal and meridional mean moisture (MSE) advection by the MJO circulation (i.e., $-\overrightarrow{\boldsymbol{v}'}\cdot\nabla\underline{h}$ in Figure 10a). Meanwhile, the enhanced westward zonal moisture gradient over the WP prefers the westward propagating WPIM by enhanced moistening through $-\overrightarrow{\boldsymbol{v}'}\cdot\nabla\underline{h}$ west of WPIM convection.

The spatial structures revealed in Figure 12 resemble the salient structure of El Niño-Southern Oscillation (ENSO) extremes, for example, with years of strong MJO propagation having a more El Niño-like large-scale structure and years of strong WPIM propagation having a more La Niña-like large-scale structure. DeMott et al. (2018) also showed that the large-scale background state conditions for strong MJO propagating events versus MJO events terminating at the Maritime Continent have similar structures. Therefore, it is possible that the interannual variability we are detecting related to strong MJO and WPIM years is impacted by the strength of ENSO.

To further highlight this potential relationship, correlations between commonly used ENSO indices and both the MJO propagation index and the WPIM propagation index are displayed in Table 1. The ENSO indices used include Niño 1 + 2, Niño 3, Niño 3.4, Niño 4, the Southern Oscillation Index (Jones, 1989), Oceanic Niño Index, Trans-Niño Index (Trenberth & Stepaniak, 2001), and Multivariate ENSO Index (Wolter & Timlin, 1993, 1998). It appears that there is a stronger interannual relationship between ENSO amplitude and WPIM propagation than between ENSO amplitude and MJO propagation (e.g., Yang et al., 2008), with all ENSO indices having correlations with the WPIM above a magnitude of 0.5 (maximum of −0.59 between Multivariate ENSO Index and WPIM) except Niño 4 and the Trans-Niño Index. This ENSO-WPIM relationship may help explain the horizontal structure of the background moisture and zonal wind fields shown in Figure 12, but it is worth recognizing that these ENSO indices may not fully capture the interannual relationship between the MJO and the WPIM, especially because they are for specific longitudes over the equatorial Pacific. A more exhaustive analysis of the relationship between

Table 1
Correlation Between Various Seasonal Mean ENSO Indices and the MJO Propagation Index and the WPIM Propagation Index for November–April 1979–2016

ENSO index	MJO propagation index	WPIM propagation index
Niño 1 + 2	0.15	**−0.51**
Niño 3	0.30	**−0.54**
Niño 3.4	0.41	**−0.54**
Niño 4	0.46	−0.40
Southern Oscillation Index	−0.40	**0.53**
Oceanic Niño Index	0.43	**−0.56**
Trans-Niño Index	−0.41	0.07
Multivariate ENSO Index	0.41	**−0.59**

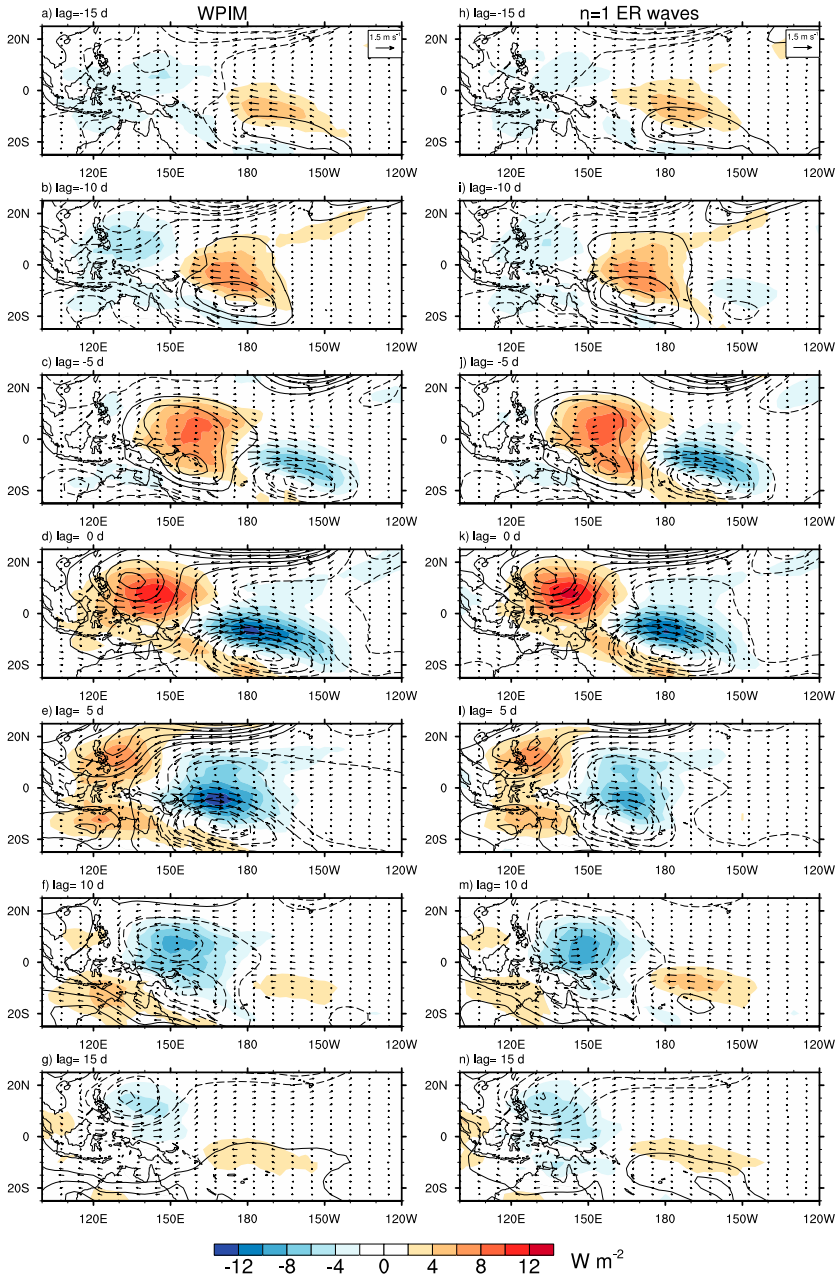

Figure 13. Unfiltered anomalies of OLR (shading), 850-hPa geopotential height (contour lines), and 850-hPa horizontal wind (vectors) lag regressed onto PC 4 (WPIM) and PC 1 of an OLR EEOF analysis for $n = 1$ ER waves. The PCs are normalized, and the lag regressions are multiplied by −1 standard deviation of their respective PCs. The geopotential height contour lines are from −8 to 8 m, the contour interval is 0.8 m, the zero line is omitted, and negative isolines are dashed.

ENSO and the MJO and WPIM is left for a follow-up study on interannual variability of the MJO and WPIM over the tropical WP.

6. Potential Origins of the WPIM

While the WPIM is discussed in this study in the context of moisture mode theory under a specific environment over the western Pacific, we recognize that it might be related to $n = 1$ ER waves, due to its similar time and space scales and its westward propagation. If this is the case, the westward propagation of the WPIM

could be explained by the beta effect with modifications by coupling with the convective processes, and moisture preconditioning may not be necessary for its westward propagation. The primary objective of this study is to illustrate how the prevalence of the eastward or westward propagating intraseasonal convection over the WP is regulated by the large-scale environment; therefore, a detailed comparison between the ER waves and the WMIP mode is not our main focus. Nevertheless, we have conducted some preliminary work in comparing these propagating modes that can be extended in a future study.

To perform this analysis, we first conducted an EEOF analysis that is exactly the same as the one discussed in this paper except instead of doing an EEOF analysis on the 15–100-day band-pass-filtered OLR anomalies; we have done it for the $n = 1$ ER wave-filtered (15–96 days, westward zonal wave numbers 1 to 6) OLR anomalies. The first two eigenvalues are well separated from the others, and the EEOFs and PCs represent the salient features of ER waves. The time evolution of OLR and 850-hPa zonal wind for the WPIM and $n = 1$ ER waves is shown in Figure 13. The spatial structure of the WPIM bears resemblance to that of the $n = 1$ ER waves presented in Kiladis et al. (2009), which they note has a broader spectral filter than many studies preceding it in that does not cut through the roughly 30-day spectral peak observed in the power spectra of brightness temperature or OLR (Figure 2). The lag-averaged (lags −15 to 15) pattern correlations between the OLR, geopotential, zonal wind, and meridional wind, of the WPIM and $n = 1$ ER waves are 0.93, 0.92, 0.92, and 0.93, respectively. Also, the correlation between the PC time series amplitude for the WPIM ($\sqrt{\text{PC3*PC3 + PC4*PC4}}$) and $n = 1$ ER waves ($\sqrt{\text{PC1*PC1 + PC2*PC2}}$) is 0.83. From these preliminary results, it seems that the WMIP mode illustrated in this study is largely similar to the $n = 1$ ER waves.

While it is possible that the WPIM could be induced by Rossby wave dynamics and modified by convective coupling as previously discussed, it could also be the case that the $n = 1$ ER wave as identified in the wave number-frequency domain actually represents a moisture mode like the MJO but it is dominated by westward propagation under the unique environment over the WP (e.g., the decreasing mean moisture beyond the Maritime Continent and prevailing low-level mean easterlies near the equator). This is reminiscent of the long-standing argument regarding the role of Kelvin wave dynamics in the eastward propagation of the MJO (Kikuchi et al., 2018; Roundy, 2008; Roundy, 2012). A more detailed comparison between the WPIM and $n = 1$ ER waves should be carried out. For example, it would be beneficial to analyze the vorticity budget of the WPIM to see if it shares the same propagation mechanism as ER waves.

7. Summary and Conclusions

The Madden-Julian oscillation (MJO), a dominant intraseasonal variability mode of tropical atmosphere, has received extensive attention in the scientific community due to its tremendous influences on global climate and weather extremes. In this study, in addition to the eastward propagating MJO, we illustrate that a westward propagating intraseasonal mode with a similar timescale as the MJO is also frequently observed over the equatorial WP during boreal winter. This westward propagating intraseasonal mode (WPIM) has a period of about 25 days and a spatial scale of wave number 3–4. It is often initiated to the east of the Dateline near 10°S and travels west-northwestward near the equator eventually dissipating near the Philippines before reaching the Indian Ocean. The vertical structures associated with the WPIM in vertical velocity and specific humidity do not exhibit significant backward tilting with height as they do for the MJO.

We apply the moisture mode framework by viewing the column MSE as a proxy of intraseasonal convection for both the MJO and the WPIM, and budget analyses of the column-integrated MSE are conducted for both the MJO and WPIM to explore key processes underlying the distinct convective propagation characteristics of these two intraseasonal modes. While the radiative heating tends to produce westward propagation tendencies for both the MJO and WPIM, it is found that both the eastward propagation of the MJO and westward propagation of the WPIM are regulated by the horizontal MSE advection. For the MJO, as reported in many recent studies, its eastward propagation is primarily driven by strong moistening to the east and drying to the west of the MJO through advection of the mean MSE by anomalous MJO circulation, with partial contributions from horizontal MSE advection by synoptic eddies and vertical MSE advection. For the WPIM, the horizontal MSE advection, which is dominated by both background wind advection of the intraseasonal MSE anomalies and advection of the background MSE by the anomalous WPIM circulation, generates moistening to the west and drying to the east of WPIM convection along with a small, secondary contribution by radiative effects, thus leading to the westward propagation of the WPIM.

Motivated by the results of the MSE budgets and Hovmöller diagrams such as Figure 1, interannual variability in zonal propagation features of intraseasonal oscillation over the WP associated with the MJO and WPIM during 37 winter seasons is further analyzed. A robust anticorrelation of −0.75 is found in the interannual activity between the eastward and westward propagating intraseasonal modes. When the eastward propagating MJO is active over the WP during a particular winter, activity of the WPIM tends to be suppressed, and vice versa. This anticorrelation between westward and eastward propagating intraseasonal variability has also been shown during boreal summer over the South China Sea (e.g., Kajikawa & Yasunari, 2005; Liu et al., 2016; Yang et al., 2008).

An analysis of large-scale conditions associated with both individual strong MJO propagation years and strong WPIM propagation years suggest that the WPIM activity over the WP is favored during periods when the equatorial low-level mean easterlies over the western and central Pacific between 150°E and 160°W are enhanced, and low-level moisture along the equator is reduced near the Dateline while enhanced over the off-equatorial regions over the WP between 110°E and 150°E. These anomalous conditions in the large-scale low-level wind and moisture fields promote the moistening/drying processes associated with the WPIM by enhanced mean easterlies over the WP while weakening the moistening/drying effects for the MJO propagation by reducing both zonal and meridional mean moisture or MSE gradient over the WP. The mean state conditions favorable for the propagation of the WPIM are strongest mainly east of the Indian Ocean, which may help explain why the WPIM weakens significantly before reaching the Indian Ocean. A preliminary analysis suggests that ENSO may play a significant role in the interannual variability of intraseasonal convective events, in agreement with DeMott et al. (2018).

Moisture coupling plays a role in the maintenance of the WPIM, possibly making it unstable through radiative effects in a similar manner as the MJO; radiative fluxes induce a slight westward positive MSE tendency (e.g., Figures 8d and 8j) and also have a large positive projection onto the column-integrated MSE (not shown). We discuss the possible origins of the WPIM and find some similarities with the physical structures of $n = 1$ ER waves. However, much more work must be done to examine the relationship between the WPIM and ER waves. A more detailed examination on the relationship between the WPIM and ER waves (and other equatorial waves) and the role of ENSO will provide important insight into the large-scale factors in regulating convectively coupled equatorial wave activity; this is left for future work.

Low-frequency fluctuations of these large-scale conditions over the Maritime Continent and Pacific Ocean, such as moisture gradients and low-level mean winds, help determine the dominance of the eastward or westward propagation of the intraseasonal mode in the region, that is, the MJO or WPIM. Since the WPIM frequently occurs over the WP with strong interference with the MJO's eastward propagation over the WP, it possibly exerts significant influences on downstream weather extremes and even the middle-to-high-latitude systems through Rossby wave teleconnections. Therefore, it would be beneficial to assess how these westward propagating WPIM events and their interactions with the MJO over the WP are represented in the present-day climate and weather forecast models.

Acknowledgments
The NOAA OLR data were obtained from https://www.esrl.noaa.gov/psd/data/gridded/data.interp_OLR.html, the ERA-Interim data from http://apps.ecmwf.int/datasets/data/interim-full-daily/levtype=sfc/, and monthly ENSO indices from https://www.esrl.noaa.gov/psd/enso/. The authors are deeply indebted to G. N. Kiladis and two anonymous reviewers. In addition, we acknowledge B. Wolding, C. DeMott, D. Kim, J. Dias, F. Ahmed, J. D. Neelin, and D. Baranowski for fruitful conversations about this work. The authors are supported by the NOAA Climate Program Office under awards NA15OAR4310098, NA15OAR4310177, and NA17OAR4310261. The data and scripts for all of the figures produced in this study are available from the repository: https://iastate.box.com/v/isv-repository.

References

Adames, Á. F., & Kim, D. (2016). The MJO as a dispersive, convectively coupled moisture wave: Theory and observations. *Journal of the Atmospheric Sciences*, *73*(3), 913–941. https://doi.org/10.1175/JAS-D-15-0170.1

Adames, Á. F., & Wallace, J. M. (2015). Three-dimensional structure and evolution of the moisture field in the MJO. *Journal of the Atmospheric Sciences*, *72*(10), 3733–3754. https://doi.org/10.1175/JAS-D-15-0003.1

Ahn, M.-S., Kim, D., Sperber, K. R., Kang, I.-S., Maloney, E., Waliser, D., & Hendon, H. (2017). MJO simulation in CMIP5 climate models: MJO skill metrics and process-oriented diagnosis. *Climate Dynamics*, *49*(11-12), 4023–4045. https://doi.org/10.1007/s00382-017-3558-4

Andersen, J. A., & Kuang, Z. (2012). Moist static energy budget of MJO-like disturbances in the atmosphere of a zonally symmetric aquaplanet. *Journal of Climate*, *25*(8), 2782–2804. https://doi.org/10.1175/JCLI-D-11-00168.1

Benedict, J. J., Pritchard, M. S., & Collins, W. D. (2015). Sensitivity of MJO propagation to a robust positive Indian Ocean dipole event in the superparameterized CAM. *Journal of Advances in Modeling Earth Systems*, *7*, 1901–1917. https://doi.org/10.1002/2015MS000530

Benjamini, Y., & Hochberg, Y. (1995). Controlling the false discovery rate: A practical and powerful approach to multiple testing. *Journal of the Royal Statistical Society*, *57*(1), 289–300. https://doi.org/10.1111/j.2517-6161.1995.tb02031.x

Bretherton, C. S., Widmann, M., Dymnikov, V. P., Wallace, J. M., & Bladé, I. (1999). The effective number of spatial degrees of freedom of a time-varying field. *Journal of Climate*, *12*(7), 1990–2009. https://doi.org/10.1175/1520-0442(1999)012<1990:TENOSD>2.0.CO;2

Cai, Q., Zhang, G. J., & Zhou, T. (2013). Impacts of shallow convection on MJO simulation: A moist static energy and moisture budget analysis. *Journal of Climate*, *26*(8), 2417–2431. https://doi.org/10.1175/JCLI-D-12-00127

Chikira, M. (2014). Eastward-propagating intraseasonal oscillation represented by Chikira Sugiyama parameterization. Part II: Understanding moisture variation under weak temperature gradient balance. *Journal of the Atmospheric Sciences*, *71*(2), 615–639. https://doi.org/10.1175/JAS-D-13038.1

Dee, D. P., Uppala, S. M., Simmons, A. J., Berrisford, P., Poli, P., Kobayashi, S., et al. (2011). The ERA-Interim reanalysis: Configuration and performance of the data assimilation system. *Quarterly Journal of the Royal Meteorological Society*, *137*(656), 553–597. https://doi.org/10.1002/qj.828

DeMott, C. A., Wolding, B. O., Maloney, E. D., & Randall, D. (2018). Atmospheric mechanisms for MJO decay over the Maritime Continent. *Journal of Geophysical Research: Atmospheres*, *123*(10), 5188–5204. https://doi.org/10.1029/2017JD026979

Dias, J., Sakaeda, N., Kiladis, G. N., & Kikuchi, K. (2017). Influences of the MJO on the space-time organization of tropical convection. *Journal of Geophysical Research: Atmospheres*, *122*, 8012–8032. https://doi.org/10.1002/2017JD026526

Duchon, C. E. (1979). Lanczos filtering in one and two dimensions. *Journal of Applied Meteorology*, *18*(8), 1016–1022. https://doi.org/10.1175/1520-0450(1979)018<1016:LFIOAT>2.0.CO;2

Feng, J., Li, T., & Zhu, W. (2015). Propagating and nonpropagating MJO events over Maritime Continent. *Journal of Climate*, *28*(21), 8430–8449. https://doi.org/10.1175/JCLI-D-15-0085.1

Fuchs, Ž., & Raymond, D. J. (2017). A simple model of intraseasonal oscillations. *Journal of Advances in Modeling Earth Systems*, *9*, 1195–1211. https://doi.org/10.1002/2017MS000963

Fuchs-Stone, Ž., Raymond, D. J., & Sentić, S. (2019). A simple model of convectively coupled equatorial Rossby waves. *Journal of Advances in Modeling Earth Systems*, *11*, 173–184. https://doi.org/10.1029/2018MS001433

Gill, A. E. (1980). Some simple solutions for heat-induced tropical circulation. *Quarterly Journal of the Royal Meteorological Society*, *106*(449), 447–462. https://doi.org/10.1002/qj.49710644905

Gilman, D. L., Fuglister, F. J., & Mitchell, J. M. (1963). On the power spectrum of "red noise". *Journal of the Atmospheric Sciences*, *20*(2), 182–184. https://doi.org/10.1175/1520-0469(1963)020<0182:OTPSON>2.0.CO;2

Gonzalez, A. O., & Jiang, X. (2017). Winter mean lower tropospheric moisture over the Maritime Continent as a climate model diagnostic metric for the propagation of the Madden-Julian oscillation. *Geophysical Research Letters*, *44*, 2588–2596. https://doi.org/10.1002/2016GL072430

Hendon, H. H., & Liebmann, B. (1994). Organization of convection within the Madden-Julian oscillation. *Journal of Geophysical Research*, *99*(D4), 8073–8083. https://doi.org/10.1029/94JD00045

Hsu, P., & Li, T. (2012). Role of the boundary layer moisture asymmetry in causing the eastward propagation of the Madden-Julian oscillation. *Journal of Climate*, *25*(14), 4914–4931. https://doi.org/10.1175/JCLI-D-11-00310.1

Hung, M.-P., Lin, J.-L., Wang, W., Kim, D., Shinoda, T., & Weaver, S. J. (2013). MJO and convectively coupled equatorial waves simulated by CMIP5 climate models. *Journal of Climate*, *26*(17), 6185–6214. https://doi.org/10.1175/JCLI-D-12-00541.1

Hurrell, J., Meehl, G. A., Bader, D., Delworth, T. L., Kirtman, B., & Wielicki, B. (2009). A unified modeling approach to climate system prediction. *Bulletin of the American Meteorological Society*, *90*(12), 1819–1832. https://doi.org/10.1175/2009BAMS2752.1

Inoue, K., & Back, L. (2015). Column-integrated moist static energy budget analysis on various time scales during TOGA COARE. *Journal of the Atmospheric Sciences*, *72*(5), 1856–1871. https://doi.org/10.1175/JAS-D-14-0249.1

Jiang, X. (2017). Key processes for the eastward propagation of the Madden-Julian oscillation based on multi-model simulations. *Journal of Geophysical Research: Atmospheres*, *122*, 755–770. https://doi.org/10.1002/2016JD025955

Jiang, X., Waliser, D. E., Olson, W. S., Tao, W.-K., L'Ecuyer, T. S., Li, K.-F., et al. (2011). Vertical diabatic heating structure of the MJO: Intercomparison between recent reanalyses and TRMM estimates. *Monthly Weather Review*, *139*(10), 3208–3223. https://doi.org/10.1175/2011mwr3636.1

Jiang, X., Waliser, D. E., Xavier, P. K., Petch, J., Klingaman, N. P., Woolnough, S. J., et al. (2015). Vertical structure and physical processes of the Madden-Julian oscillation: Exploring key model physics in climate simulations. *Journal of Geophysical Research: Atmospheres*, *120*, 4718–4748. https://doi.org/10.1002/2014JD022375

Jiang, X., Zhao, M., Maloney, E. D., & Waliser, D. E. (2016). Convective moisture adjustment time scale as a key factor in regulating model amplitude of the Madden-Julian oscillation. *Geophysical Research Letters*, *43*, 10,412–10,419. https://doi.org/10.1002/2016GL070898

Jones, P. D. (1989). The influence of ENSO on global temperatures. *Climate Monitoring*, *17*, 80–89.

Kajikawa, Y., & Yasunari, T. (2005). Interannual variability of the 10–25- and 30–60-day variation over the South China Sea during boreal summer. *Geophysical Research Letters*, *32*, L04710. https://doi.org/10.1029/2004GL021836

Keen, R. A. (1982). The role of cross-equatorial tropical cyclone pairs in the Southern Oscillation. *Monthly Weather Review*, *110*(10), 1405–1416. https://doi.org/10.1175/1520-0493(1982)110<1405:TROCET>2.0.CO;2

Kikuchi, K., Kiladis, G. N., Dias, J., & Nasuno, T. (2018). Convectively coupled equatorial waves within the MJO during CINDY/DYNAMO: Slow Kelvin waves as building blocks. *Climate Dynamics*, *50*(11-12), 4211–4230. https://doi.org/10.1007/s00382-017-3869-5

Kikuchi, K., & Takayabu, Y. N. (2004). The development of organized convection associated with the MJO during TOGA COARE IOP: Trimodal characteristics. *Geophysical Research Letters*, *31*, L10101. https://doi.org/10.1029/2004GL019601

Kikuchi, K., & Wang, B. (2010). Spatiotemporal wavelet transform and the multiscale behavior of the Madden-Julian oscillation. *Journal of Climate*, *23*(14), 3814–3834. https://doi.org/10.1175/2010JCLI2693.1

Kiladis, G. N. (1998). Observations of Rossby waves linked to convection over the eastern tropical Pacific. *Journal of the Atmospheric Sciences*, *55*(3), 321–339. https://doi.org/10.1175/1520-0469(1998)055<0321:OORWLT>2.0.CO;2

Kiladis, G. N., Meehl, G. A., & Weickmann, K. M. (1994). Large-scale circulation associated with westerly wind bursts and deep convection over the western equatorial Pacific. *Journal of Geophysical Research*, *99*(D9), 18,527–18,544. https://doi.org/10.1029/94JD01486

Kiladis, G. N., Straub, K. H., & Haertel, P. T. (2005). Zonal and vertical structure of the Madden–Julian oscillation. *Journal of the Atmospheric Sciences*, *62*(8), 2790–2809. https://doi.org/10.1175/JAS3520.1

Kiladis, G. N., & Wheeler, M. (1995). Horizontal and vertical structure of observed tropospheric equatorial Rossby waves. *Journal of Geophysical Research*, *100*(D11), 22,981–22,997. https://doi.org/10.1029/95JD02415

Kiladis, G. N., Wheeler, M. C., Haertel, P. T., Straub, K. H., & Roundy, P. E. (2009). Convectively coupled equatorial waves. *Reviews of Geophysics*, *47*, RG2003. https://doi.org/10.1029/2008RG000266

Kim, D., Kim, H., & Lee, M.-I. (2017). Why does the MJO detour the Maritime Continent during austral summer? *Geophysical Research Letters*, n/a–n/a. https://doi.org/10.1002/2017GL072643

Kim, D., Kug, J.-S., & Sobel, A. H. (2014). Propagating versus nonpropagating Madden-Julian oscillation events. *Journal of Climate*, *27*(1), 111–125. https://doi.org/10.1175/JCLI-D-13-00084.1

Kim, H.-M. (2017). The impact of the mean moisture bias on the key physics of MJO propagation in the ECMWF reforecast. *Journal of Geophysical Research: Atmospheres*, *122*, 7772–7784. https://doi.org/10.1002/2017JD027005

Kiranmayi, L., & Maloney, E. D. (2011). Intraseasonal moist static energy budget in reanalysis data. *Journal of Geophysical Research*, *116*, D21117. https://doi.org/10.1029/2011JD016031

Liebmann, B., & Smith, C. A. (1996). Description of a complete (interpolated) outgoing longwave radiation dataset. *Bulletin of the American Meteorological Society*, *77*, 1275–1277.
Liu, F., Li, T., Wang, H., Deng, L., & Zhang, Y. (2016). Modulation of boreal summer intraseasonal oscillations over the western north Pacific by ENSO. *Journal of Climate*, *29*(20), 7189–7201. https://doi.org/10.1175/JCLI-D-15-0831.1
Madden, R. A., & Julian, P. R. (1971). Detection of a 40–50 day oscillation in the zonal wind in the tropical Pacific. *Journal of the Atmospheric Sciences*, *28*(5), 702–708. https://doi.org/10.1175/1520-0469(1971)028(0702:DOADOI)2.0.CO;2
Madden, R. A., & Julian, P. R. (1972). Description of global-scale circulation cells in the tropics with a 40–50 day period. *Journal of the Atmospheric Sciences*, *29*(6), 1109–1123. https://doi.org/10.1175/1520-0469(1972)029(1109:DOGSCC)2.0.CO;2
Maloney, E. D. (2009). The moist static energy budget of a composite tropical intraseasonal oscillation in a climate model. *Journal of Climate*, *22*(3), 711–729. https://doi.org/10.1175/2008JCLI2542.1
Mapes, B. E., & Bacmeister, J. T. (2012). Diagnosis of tropical biases and the MJO from patterns in the MERRA analysis tendency fields. *Journal of Climate*, *25*(18), 6202–6214. https://doi.org/10.1175/JCLI-D-11-00424.1
Mapes, B. E., Tulich, S., Lin, J., & Zuidema, P. (2006). The mesoscale convection life cycle: Building block or prototype for large-scale tropical waves? *Dynamics of Atmospheres and Oceans*, *42*(1-4), 3–29. https://doi.org/10.1016/j.dynatmoce.2006.03.003
Matsuno, T. (1966). Quasi-geostrophic motions in the equatorial area. *Journal of the Meteorological Society of Japan*, *44*(1), 25–43. https://doi.org/10.2151/jmsj1965.44.1_25
Nakazawa, T. (1988). Tropical super clusters within intraseasonal variations over the western Pacific. *Meteorological Society of Japan*, *66*(6), 823–839. https://doi.org/10.2151/jmsj1965.66.6_823
Nasuno, T., Li, T., & Kikuchi, K. (2015). Moistening processes before the convective initiation of Madden-Julian oscillation events during the CINDY2011/DYNAMO period. *Monthly Weather Review*, *143*, 622–643. https://doi.org/10.1175/MWR-D-14-00132.1
Neena, J. M., Lee, J. Y., Waliser, D., Wang, B., & Jiang, X. (2014). Predictability of the Madden Julian oscillation in the Intraseasonal Variability Hindcast Experiment (ISVHE). *Journal of Climate*, *27*(12), 4531–4543. https://doi.org/10.1175/JCLI-D-13-00624.1
North, G. R., Bell, T. L., Cahalan, R. F., & Moeng, F. J. (1982). Sampling errors in the estimation of empirical orthogonal functions. *Monthly Weather Review*, *110*(7), 699–706. https://doi.org/10.1175/1520-0493(1982)110<0699:SEITEO>2.0.CO;2
Numaguti, A. (1995). Characteristics of 4-to-20-day-period disturbances observed in the equatorial Pacific during the TOGA COARE IOP. *Journal of the Meteorological Society of Japan*, *73*(2B), 353–377. https://doi.org/10.2151/jmsj1965.73.2B_353
Pires, P., Redelsperger, J., & Lafore, J. (1997). Equatorial atmospheric waves and their association to convection. *Monthly Weather Review*, *125*(6), 1167–1184. https://doi.org/10.1175/1520-0493(1997)125<1167:EAWATA>2.0.CO;2
Pritchard, M. S., & Bretherton, C. S. (2014). Causal evidence that rotational moisture advection is critical to the superparameterized Madden-Julian oscillation. *Journal of the Atmospheric Sciences*, *71*(2), 800–815. https://doi.org/10.1175/JAS-D-13-0119.1
Raymond, D. J. (2001). A new model of the Madden-Julian oscillation. *Journal of the Atmospheric Sciences*, *58*(18), 2807–2819. https://doi.org/10.1175/1520-0469(2001)058<2807:ANMOTM>2.0.CO;2
Raymond, D. J., & Fuchs, Ž. (2009). Moisture modes and the Madden-Julian oscillation. *Journal of Climate*, *22*(11), 3031–3046. https://doi.org/10.1175/2008JCLI2739.1
Roundy, P. E. (2008). Analysis of convectively coupled Kelvin waves in the Indian ocean MJO. *Journal of the Atmospheric Sciences*, *65*(4), 1342–1359. https://doi.org/10.1175/2007jas2345.1
Roundy, P. E. (2012). Observed structure of convectively coupled waves as a function of equivalent depth: Kelvin waves and the Madden-Julian oscillation. *Journal of the Atmospheric Sciences*, *69*(7), 2097–2106. https://doi.org/10.1175/JAS-D-12-03.1
Roundy, P. E., & Frank, W. M. (2004a). Effects of low-frequency wave interactions on intraseasonal oscillations. *Journal of the Atmospheric Sciences*, *61*(24), 3025–3040. https://doi.org/10.1175/JAS-3348.1
Roundy, P. E., & Frank, W. M. (2004b). Applications of a multiple linear regression model to the analysis of relationships between eastward- and westward-moving intraseasonal modes. *Journal of the Atmospheric Sciences*, *61*(24), 3041–3048. https://doi.org/10.1175/JAS-3349.1
Salby, M. L., & Hendon, H. H. (1994). Intraseasonal behavior of clouds, temperature, and motion in the tropics. *Journal of the Atmospheric Sciences*, *51*(15), 2207–2224. https://doi.org/10.1175/1520-0469(1994)051<2207:IBOCTA>2.0.CO;2
Schubert, W. H., & Masarik, M. T. (2006). Potential vorticity aspects of the MJO. *Dynamics of Atmospheres and Oceans*, *42*(1-4), 127–151. https://doi.org/10.1016/j.dynatmoce.2006.02.003
Serra, Y. L., Jiang, X., Tian, B., Amador-Astua, J., Maloney, E. D., & Kiladis, G. N. (2014). Tropical intraseasonal modes of the atmosphere. *Annual Review of Environment and Resources*, *39*(1), 189–215. https://doi.org/10.1146/annurev-environ-020413-134219
Sobel, A., & Maloney, E. (2012). An idealized semi-empirical framework for modeling the Madden-Julian oscillation. *Journal of the Atmospheric Sciences*, *69*(5), 1691–1705. https://doi.org/10.1175/JAS-D-11-0118.1
Sobel, A., & Maloney, E. (2013). Moisture modes and the eastward propagation of the MJO. *Journal of the Atmospheric Sciences*, *70*(1), 187–192. https://doi.org/10.1175/JAS-D-12-0189.1
Sobel, A., Wang, S., & Kim, D. (2014). Moist static energy budget of the MJO during DYNAMO. *Journal of the Atmospheric Sciences*, *71*(11), 4276–4291. https://doi.org/10.1175/JAS-D-14-0052.1
Sobel, A. H., Nilsson, J., & Polvani, L. M. (2001). The weak temperature gradient approximation and balanced tropical moisture waves. *Journal of the Atmospheric Sciences*, *58*(23), 3650–3665. https://doi.org/10.1175/1520-0469(2001)058<3650:TWTGAA>2.0.CO;2
Tian, B., Waliser, D. E., Fetzer, E. J., & Yung, Y. L. (2010). Vertical moist thermodynamic structure of the Madden–Julian oscillation in Atmospheric Infrared Sounder retrievals: An update and a comparison to ECMWF Interim re-analysis. *Monthly Weather Review*, *138*(12), 4576–4582. https://doi.org/10.1175/2010MWR3486.1
Trenberth, K. E., & Stepaniak, D. P. (2001). Indices of El Niño evolution. *Journal of Climate*, *14*(8), 1697–1701. https://doi.org/10.1175/1520-0442(2001)014<1697:LIOENO>2.0.CO;2
Vitart, F., Ardilouze, C., Bonet, A., Brookshaw, A., Chen, M., Codorean, C., et al. (2017). The Subseasonal to Seasonal (S2S) prediction project database. *Bulletin of the American Meteorological Society*, *98*(1), 163–173. https://doi.org/10.1175/BAMS-D-16-0017.1
Vitart, F., & Molteni, F. (2010). Simulation of the Madden-Julian oscillation and its teleconnections in the ECMWF forecast system. *Quarterly Journal of the Royal Meteorological Society*, *136*(649), 842–855. https://doi.org/10.1002/qj.623
Waliser, D., Weickmann, K., Dole, R., Schubert, S., Alves, O., Jones, C., et al. (2006). The experimental MJO prediction project. *Bulletin of the American Meteorological Society*, *87*(4), 425–431. https://doi.org/10.1175/BAMS-87-4-425
Wang, L., Li, T., Maloney, E., & Wang, B. (2017). Fundamental causes of propagating and nonpropagating MJOs in MJOTF/GASS models. *Journal of Climate*, *30*(10), 3743–3769. https://doi.org/10.1175/jcli-d-16-0765.1
Weare, B. C., & Nasstrom, J. S. (1982). Examples of extended empirical orthogonal function analyses. *Monthly Weather Review*, *110*(6), 481–485. https://doi.org/10.1175/1520-0493(1982)110<0481:EOEEOF>2.0.CO;2

Wheeler, M., & Kiladis, G. N. (1999). Convectively coupled equatorial waves: Analysis of clouds and temperature in the wavenumber-frequency domain. *Journal of the Atmospheric Sciences*, *56*, 374–399. https://doi.org/10.1175/1520-0469(1999)056<0374:CCEWAO>2.0.CO;2

Wilks, D. S. (2016). "The stippling shows statistically significant grid points": How research results are routinely overstated and overinterpreted, and what to do about it. *Bulletin of the American Meteorological Society*, *97*(12), 2263–2273. https://doi.org/10.1175/BAMS-D-15-00267.1

Wolding, B. O., Maloney, E. D., & Branson, M. (2016). Vertically resolved weak temperature gradient analysis of the Madden-Julian oscillation in SP-CESM. *Journal of Advances in Modeling Earth Systems*, *8*, 1586–1619. https://doi.org/10.1002/2016MS000724

Wolter, K., and M. S. Timlin, 1993: Monitoring ENSO in COADS with a seasonally adjusted principal component index. *Proc. 17th Climate Diagnostics Workshop*, Norman, OK, NOAA/NMC/CAC, 52–57. [Available from Klaus Wolter (kew@cdc.noaa.gov)].

Wolter, K., & Timlin, M. S. (1998). Measuring the strength of ENSO events: How does 1997/98 rank? *Weather*, *53*(9), 315–324. https://doi.org/10.1002/j.1477-8696.1998.tb06408.x

Yang, J., Wang, B., & Wang, B. (2008). Anticorrelated intensity change of the quasi–biweekly and 30–50-day oscillations over the South China Sea. *Geophysical Research Letters*, *35*, L16702. https://doi.org/10.1029/2008GL034449

Yokoi, S., & Sobel, A. H. (2015). Intraseasonal variability and seasonal march of the moist static energy budget over the eastern Maritime Continent during CINDY2011/DYNAMO. *Journal of the Meteorological Society of Japan Series II*, *93A*(0), 81–100. https://doi.org/10.2151/jmsj.2015-041

Yu, J., & Neelin, J. D. (1994). Modes of tropical variability under convective adjustment and the Madden–Julian oscillation. Part II: Numerical results. *Journal of the Atmospheric Sciences*, *51*(13), 1895–1914. https://doi.org/10.1175/1520-0469(1994)051<1895:MOTVUC>2.0.CO;2

Zhang, C. (2013). Madden-Julian oscillation: Bridging weather and climate. *Bulletin of the American Meteorological Society*, *94*(12), 1849–1870. https://doi.org/10.1175/BAMS-D-12-00026.1

Zhang, C., & Ling, J. (2017). Barrier effect of the Indo-Pacific Maritime Continent on the MJO: Perspectives from tracking MJO precipitation. *Journal of Climate*, *30*(9), 3439–3459. https://doi.org/10.1175/JCLI-D-16-0614.1

Erratum

In the originally published version of this article, Figure 10 did not include the correct latitude range of 25S-5S. The figure has since been corrected, and this version may be considered the authoritative version of record.